

[Click here to view linked References](#)

1 Subgrid Variability of Atmospheric Surface-Layer Parameters 2 in Complex Terrain

3 Sebastian F. Otárola-Bustos¹ • Harindra J. S Fernando¹ • James M. Wilczak² •
4 Andrey A. Grachev³ • Christopher Hocut³ • Robert Dumais⁴

5 Received: 15 February 2022/ Accepted: DD Month 2022/ Published online: DD Month YEAR
6 © Springer Science + Business Media B. V.

7
8 **Abstract:** This paper reports analysis of eddy-covariance data collected during the WFIP2
9 field campaign in the complex-terrain of the US Pacific Northwest. A 31-day period
10 representative of the region's dry season was used to address the following questions: (1)
11 To what extent does the Constant-Flux Layer (CFL) assumption hold? (2) What is the
12 spatial variability of turbulent and momentum fluxes over km scales? and (3) How skilful
13 are the surface-layer parameterizations of mesoscale models? These questions are directly
14 relevant to subgrid parameterization studies of mesoscale models. Results show that the
15 efficacy of the CFL concept and the spatial variability of turbulent and momentum fluxes
16 are dependent on: (i) the turbulent parameter being analysed, (ii) the measurement's
17 location, (iii) the atmospheric stability regime (determined by the flow and vertical
18 stratification), and (iv) the magnitude of the flux. Finally, the skill of the physics
19 formulation of an often-used surface-layer parameterization scheme available in the
20 Weather Research and Forecasting (WRF) model was also evaluated. Meteorological
21 conditions associated with the highest and the lowest errors were identified. A metric to
22 quantify (time-dependent) flow heterogeneity is proposed, which appears to be a good
23 candidate to predict the skill of idealized surface-layer parameterization schemes in
24 complex terrain.

1

✉ Sebastian F. Otárola-Bustos
sotarola@nd.edu

¹ Department of Civil and Environmental Engineering and Earth Sciences,
University of Notre Dame, IN, USA.

² Earth System Research Laboratory, NOAA, Boulder, CO, USA.

³ Boundary Layer Research Team/Atmospheric Dynamics & Analytics Branch, DEVCOM Army
Research Laboratory, White Sands, NM, USA.

⁴ Data Assimilation and Nowcasting Team, Army Research Laboratory, NM, USA.

25 **Keywords** Constant-flux layer · Complex terrain · Parameterizations · Subgrid variability
26 · Surface-layer

27 **1 Introduction**

28
29 Complex-terrain flows cover multiple space-time scales and are associated with steep
30 gradients of meteorological variables that depend on the complexity of the terrain and
31 background forcing (Fernando 2010). Complex terrain weather has many societal
32 applications, such as, prediction of air quality (Giovannini et al. 2020), aviation hazards
33 (Gultepe et al. 2019), wildfire control (Carvalho et al. 2020), agricultural damage from
34 frost due to cold pooling (Chung et al. 2006), wind energy (Haupt et al. 2019), and
35 anomalous rainfall and flooding (Luchetti et al. 2020). These applications rely on
36 mesoscale Numerical Weather Prediction (NWP) models that use 1-30 km horizontal grid
37 sizes, where atmospheric motions such as fronts, tropical storms, land/sea breeze,
38 mountain/valley circulation, and thunderstorms can be captured (Sati and Mohan 2021).
39 Yet, microscale (1-100 m) turbulent eddies within the Atmospheric Boundary Layer (ABL)
40 that are key to the exchange of momentum, heat, and mass in the atmosphere are not
41 properly represented in NWP models (Maronga et al. 2020). In particular, terrain
42 heterogeneities (complex terrain) pose challenges for accurately calculating turbulent
43 fluxes of momentum, heat, and moisture in the Atmospheric Surface Layer (SL) (Martins
44 et al. 2009; Liang et al. 2020), wherein important interactions between the surface and air
45 aloft takes place (Wouters et al. 2012). Terrain heterogeneities can modify surface drag,
46 turbulent mixing, and heat transfer, and they can interact with the background flow at
47 multiple space-time scales, generating a wide range of meteorological phenomena
48 including but not limited to internal boundary layers, thermal winds, critical layers, lee
49 waves, and rotors (Garrat 1994; Fernando et al. 2010; Kadivar et al 2021).
50 In NWP models, turbulent fluxes as well as winds, temperature, and moisture at the lowest
51 computational level are represented using physics-based expressions known as Surface
52 Layer parameterization schemes (hereafter SL schemes) (Stull 1988; Nakanishi and Niino
53 2009; Jiménez et al. 2012a). These SL schemes rely on the assumed presence of a Constant-
54 Flux Layer (CFL) where turbulent fluxes of momentum, heat, and moisture are
55 approximately constant, and the existence of a CFL is the basis of the Monin-Obukhov
56 Similarity Theory (MOST) developed for Flat and Homogeneous Terrain (FHT) (Obukhov
57 1946; Monin and Obukhov 1954). The terms Surface Layer (SL) and CFL are used in the
58 literature interchangeably. Even for nearly idealized FHT in nature, turbulent fluxes change
59 with height, and their vertical gradients often peak near the ground where turbulent fluxes
60 tend to be the highest. As pointed out by Wyngaard (2011), nonetheless, when non-
61 dimensionalized by SL scales, these gradients become negligible, and hence the name CFL.
62 In practice, over FHT, where the applicability of MOST has been well established
63 (Panofsky and Dutton 1984; Wyngaard 2011), a CFL is said to exist over the height where

64 turbulent fluxes vary less than 10% (Kaimal and Businger 1970). Nonetheless, SL schemes
65 are employed for all types of terrain, including complex terrain, for which only a few
66 authors have explored the validity of the CFL approximation. For instance, Nadeau et al.
67 (2013) studied the vertical variability of turbulent heat and momentum fluxes over a steep
68 alpine slope (25-40°) near La Fouly, Switzerland, and Sfyri et al. (2018) did the same (with
69 the addition of water vapor fluxes) for the Inn Valley, Austria. They both reported
70 variations in turbulent fluxes that exceed by an order of magnitude validity thresholds
71 commonly used for MOST. Nadeau et al. (2013) used a 10% threshold for the first 6 meters
72 above the ground, and Sfyri et al. (2018) used a 20% threshold for the first 20 meters above
73 the ground (which was used in this study). Dan Li et al. (2018) found that when a CFL is
74 assumed in the Atmospheric Surface Layer, several constraints are imposed on high-order
75 fluxes and their gradients, thus understanding when the CFL breaks down in complex
76 terrain is of great importance, not only for its obvious impact on the skill of SL schemes.
77 This article uses eddy-covariance data obtained in an area of complex terrain of horizontal
78 dimensions comparable to a single grid cell of a mesoscale model (~ 1 - 3 km) during the
79 Second Wind Forecast Improvement Project (WFIP2) field campaign (Wilczak et al. 2019)
80 to address three research questions: (1) To what extent does the CFL approximation hold
81 in complex terrain? (2) What is the horizontal spatial variability of turbulent heat and
82 momentum fluxes in the area studied, which is within subgrid scales of mesoscale models,
83 and 3) Is the Monin-Obukhov (MO) theory developed for FHT and used by SL schemes in
84 NWP models capable of representing the friction velocity for the entire instrumented site,
85 and under what conditions it tends to fail?

86 **2 Methods**

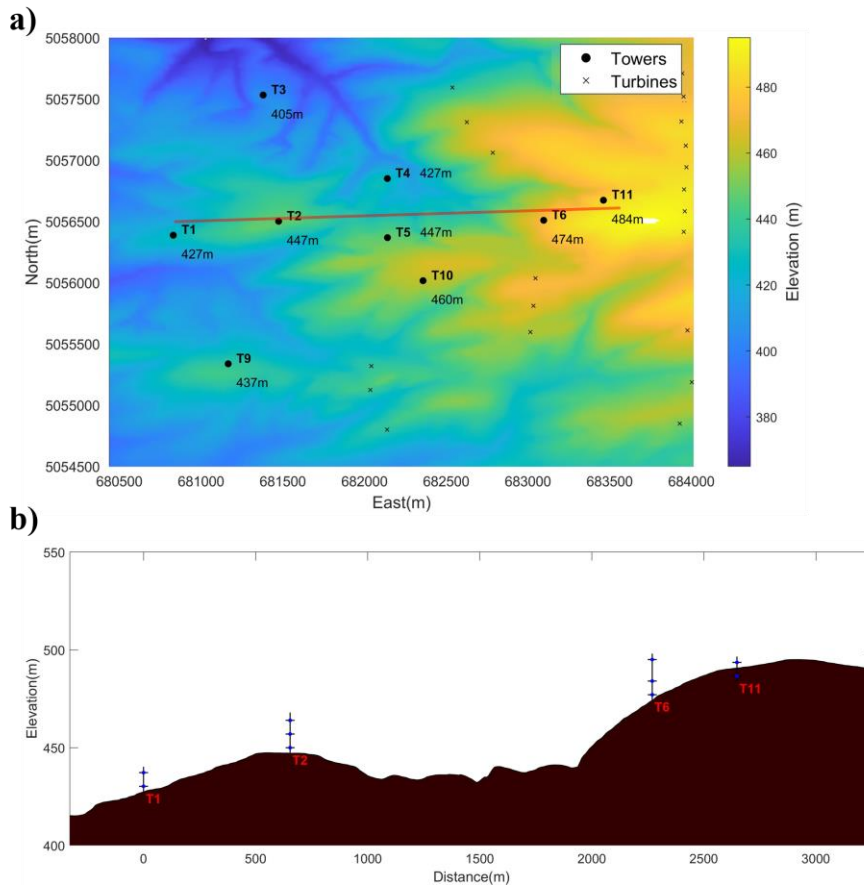
87

88 **2.1 Dataset**

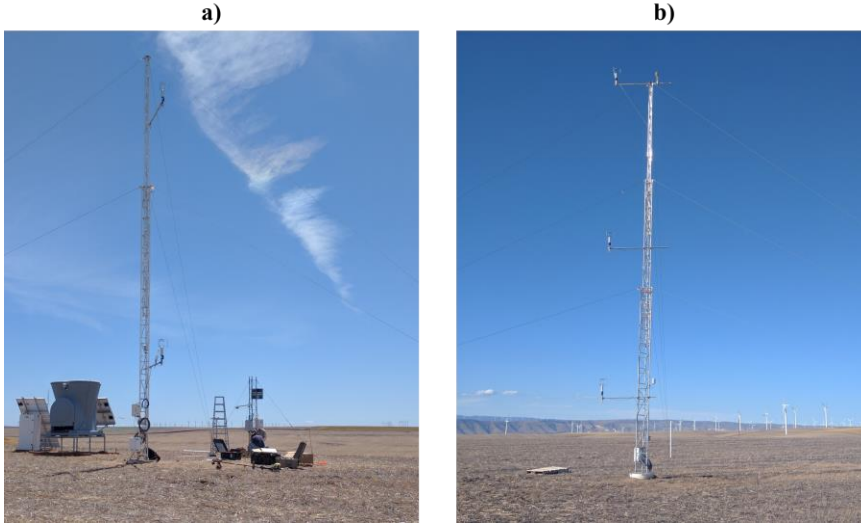
89

90 The data analyzed and discussed herein were obtained during the WFIP2 experiment that
91 took place in the Columbia River gorge and basin region of the US Pacific Northwest (OR
92 and WA) between 2015 December to 2017 January. Specifically, the three components of
93 wind velocity and sonic temperature were obtained with an array of meteorological towers
94 equipped with multiple levels of sonic anemometers (at 20 Hz). The vertical profiles of
95 wind speed and direction up to 200 m above ground level (agl) were measured with a
96 SODAR (hereafter, for brevity, agl will not be used when describing the heights).
97 The instruments covered a region of complex terrain comparable to the horizontal
98 dimensions of a single grid cell of a high-resolution Numerical Weather Prediction (NWP)
99 model ($\Delta X, \Delta Y \sim 1-5$ km). This region was located ~ 8 km southwest from Rufus (OR) and
100 5 km North from Wasco (OR). The layout of the towers and the terrain elevation are given
101 in Fig. 1a. The elevation profile of the tower transect for T1, T2, T6, and T11 (indicated by
102 the red line in Fig. 1a) is shown in Fig. 1b. The 10-m tower and the SODAR at site T1 are

103 shown in Fig. 2a, and the 21-m tower at site T6 is shown in Fig. 2b. This transect had an
104 approximately East-West (EW) direction, and it spanned a distance ~ 2.6 km, characterized
105 by an average slope of 5% and an elevation difference of 40 m. Fig. 1a and Fig. 1b were
106 generated using terrain data with $1/3$ arc seconds (~ 10 m) horizontal resolution downloaded
107 from the National Elevation Dataset (NED) at <https://nationalmap.gov>. The exact
108 coordinates, terrain elevation, type of instrumentation, and measurement heights are listed
109 in Table 1 for all sites. Additional details regarding the T1 observation site (Physics Site
110 PS01), the instrumentation, and the data can be found in Grachev et al. (2020, 2021).
111



112
113 Figure 1: (a) Colormap of Elevation for the instrumented region. Towers and wind turbines are indicated by
114 the circle and cross symbols, respectively, and the local terrain elevation is indicated for all tower sites. (b)
115 Elevation profile for East-West transect of UND towers (red line in Fig. 1a).
116



117
 118
 119
 120
 121
 122
 123

Figure 2: (a) ND tower T1 with two levels of sonic anemometers and co-located instrumentation of collaborators (SODAR and solar/soil measurements). (b) ND tower T6 with three levels of sonic anemometers.

Table 1: Tower's location, height, and elevation in meters above sea level (masl).

Tower	LAT	LON	Elevation (masl)	Sonic Levels (m)	Model	Deployed by:
T1	45.637	-120.679	428	3, 10	Young RM 8100	University of Notre Dame (UND)
T2	45.638	-120.672	445	3, 10, 17		
T6	45.6378	-120.651	475	3, 10, 21		
T11	45.6394	-120.646	484	3, 10		
T3	45.648	-120.673	405	10	Metek USA-1	Argonne National Laboratory (ANL)
T9	45.628	-120.676	439	10		
T4	45.641	-120.663	426	10	Gill R3-50	Pacific Northwest National Laboratory (PNNL)
T5	45.6369	-120.663	449	10		
T10	45.6337	-120.661	458	10		

124
 125
 126
 127
 128
 129
 130

2.2 Data Quality Control

As listed in Table 1, the operation of towers in Fig. 1 was done by multiple research organizations. To minimize uncertainties associated with different tower operators, the raw data for all towers were processed using the same quality control procedures developed for the University of Notre Dame (UND) towers. This included sequentially: (i) visual

131 inspection of data, (ii) removal of outliers, defined as points with differences higher than
 132 four standard deviations from the median, and (iii) tilt correction using the planar-fit
 133 method that aligns the sonic anemometer coordinate system into a mean streamline
 134 coordinate system to reduce crosswind errors when calculating fluxes (Wilczak et al.
 135 2001). In addition, to minimize wake effects from the towers and wind turbines located in
 136 the eastern part of the domain (Fig. 1a), only data associated with wind direction in the
 137 sector $240^\circ - 290^\circ$ was used in the statistical analysis of Sect. 3.2 and Sect. 3.3.

138

139 **2.3 Micrometeorological Conditions During Study Period**

140

141 For this study, a 31-day period between 27 August to 26 September, 2016 was selected in
 142 view of (i) the availability of a complete dataset from the towers and SODAR, (ii) presence
 143 of dry soil conditions for ABL turbulence studies, and (iii) ideal meteorological conditions
 144 for the study of CFL validity and the evaluation of SL schemes, which were identified with
 145 selected values of wind speed, wind direction (θ), and Obukhov length L , with the latter
 146 defined according to eq.1:

$$L = -\frac{u_*^3}{\kappa g \alpha Q_T}, \quad (1)$$

$$u_* = \left(\overline{u'w'^2} + \overline{v'w'^2} \right)^{\frac{1}{4}}, \quad (2)$$

$$Q_T = \overline{w'T_s'}, \quad (3)$$

$$\alpha \cong \overline{T_s}^{-1} \quad (4)$$

147

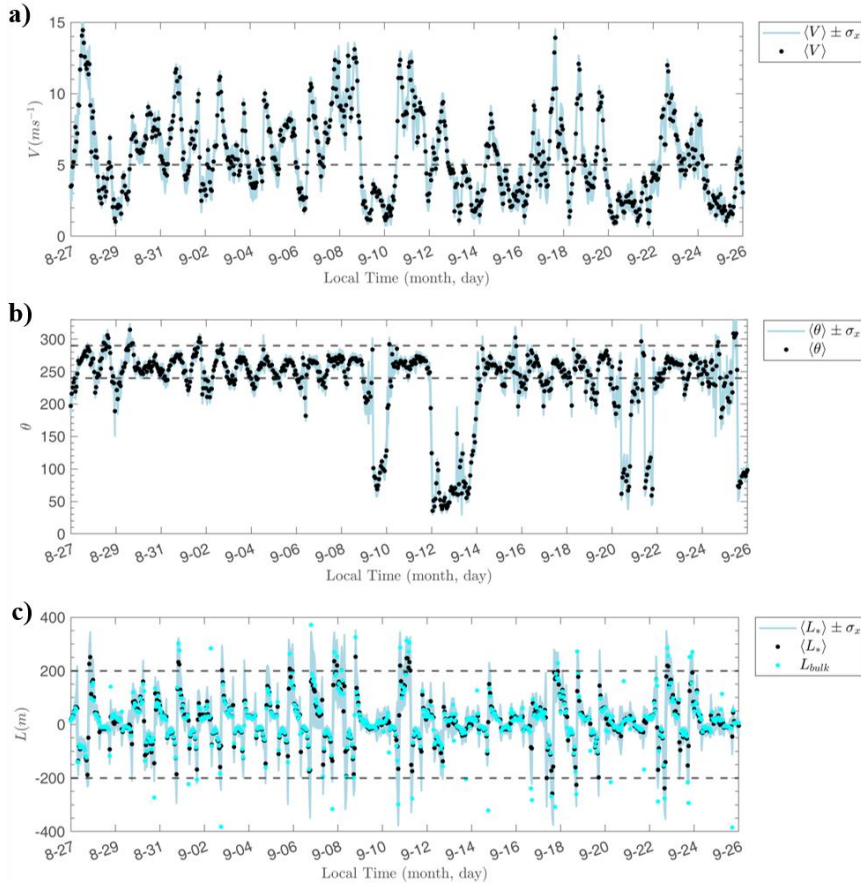
148 Where u_* is the friction velocity (defined in eq. 2), Q_T is the turbulent temperature flux
 149 (defined in eq. 3), α is the thermal expansion coefficient (defined in eq. 4), κ is the von
 150 Kármán constant, and g is the gravitational acceleration.

151 The terms $\overline{u'w'}$ and $\overline{v'w'}$ in eq. 2 correspond to the longitudinal and lateral momentum
 152 fluxes, respectively. The overbar operator indicates the covariance of high-frequency
 153 quantities ($u'w'$, $v'w'$, and $w'T_s'$) over a 15-min interval, with (u' , v' , w') and (T_s')
 154 velocity and temperature fluctuations measured with sonic anemometers, respectively.

155 In Fig. 3a-c, the black dots correspond to 15-min averaged wind speed, wind direction
 156 (theta) calculated from the averaged wind components, and Obukhov length at $z = 10$ m
 157 and spatially averaged across all 9 towers, $\langle V \rangle$, $\langle \theta \rangle$, and $\langle L \rangle$, respectively. The spatial
 158 variability of the measurements ($\langle . \rangle \pm \sigma_x$) is indicated by the light-blue shaded region.

159 The ideal meteorological conditions selected from the 31-day period used in this study
 160 included i) identifiable quiescent and transitional winds separated by a windspeed threshold
 161 of 5 m s^{-1} (dashed line in Fig. 3a), ii) frequent westerly winds in attendance and defined by
 162 wind directions in the sector $240^\circ - 290^\circ$ (indicated by the two dashed lines in Fig. 3b), and

163 iii) three distinct stability regimes based on the Obukhov length at $z = 10\text{m}$ and consistent
 164 with previous studies (Moraes et al. 2005; Tampieri et al. 2009; Munoz-Esparza et al. 2012;
 165 Sfyri et al. 2018; Bodini et al. 2019), as indicated in Table 2.



166
 167 Figure 3: Time series of (a) wind speed, (b) wind direction, and c) Obukhov length. The angular brackets $\langle \cdot \rangle$
 168 indicate the variables (V , θ , or L) were averaged in space across all 9 towers (black dots in (a)-(c)). The light-
 169 blue shaded area corresponds to the spatial standard deviation of measurements across all 9 towers (σ_x). The
 170 cyan dots in (c) correspond to a 'bulk' Obukhov length L_{bulk} . The data was smoothed with a 1-hour
 171 averaging window for convenience of visualization.

172
 173 Table 2: Stability classification based on Obukhov length scale (L) threshold and stability parameter at $z =$
 174 10m.

Class of Flow	Obukhov Length (L^*)	Stability Parameter ($\xi = zL^{-1}$)
Unstable (U),	When $-200 \leq L < 0$	$\xi \leq -0.05$
Stable (S)	When $0 < L \leq 200$	$\xi \geq 0.05$
Neutral (N)	When $ L > 200$,	$-0.05 < \xi < 0.05$

175

176 In Table 2, L is the Obukhov length in meters (eq. 1), and threshold values $L = \pm 200$ m
 177 are indicated by the two dashed lines in Fig. 3c.

178 To illustrate the spatial variability of the Obukhov length within spatial scales comparable
 179 to the finest grid-cells of mesoscale models, a bulk Obukhov length (L_{bulk}) was calculated
 180 according to eq. 5, which is analogous to eq. 1, but with spatially averaged values of u_* ,
 181 Q_T and α across all towers, as indicated by the angular brackets.

$$L_{bulk} = -\frac{\langle u^* \rangle^3}{\kappa g \langle \alpha \rangle \langle Q_T \rangle}, \quad (5)$$

182 Where $\langle u^* \rangle$ is the observed friction velocity spatially averaged across all 9 towers and
 183 calculated according to eq. 6 as:

$$\langle u^* \rangle = \frac{1}{N} \sum_{i=1}^N u^*(x_i, t), \quad (6)$$

184 Where $u^*(x_i, t)$ is the friction velocity at $z = 10$ m measured at site x_i (with $i = 1, 2, \dots, N$),
 185 with $N = 9$ the number of towers. Similarly, $\langle \alpha \rangle$ and $\langle Q_T \rangle$ are the spatially averaged
 186 thermal expansion coefficient and temperature flux across all 9 towers. Given the similarity
 187 of $\langle u^* \rangle$ to the definition of L_{bulk} , $\langle u^* \rangle$ can be thought of a ‘bulk’ friction velocity.

188 The values of L_{bulk} (cyan dots in Fig. 3c) are in general agreement with the spatially
 189 averaged values of L (black dots in Fig. 3c); however, note that during periods of high
 190 variability between the towers (high σ_x), differences between L and L_{bulk} can be
 191 important. The reasons of these differences are beyond the scope of this article and call for
 192 more detailed studies in complex terrain at small horizontal scales (1-3 km).

193

194 2.4 Evaluation of Surface Layer Schemes

195

196 The instrumented domain (Fig. 1a) was designed to study subgrid physical processes of
 197 NWP models. To this end, we aim to quantify errors introduced when using idealized SL
 198 schemes for complex terrain and to reveal how these errors vary with atmospheric
 199 conditions. One of the most popular SL schemes of the Weather Research and Forecasting
 200 (WRF) model (Skamarock et al. 2008) is WRF SL option 1 (Jiménez et al. 2012), which is
 201 an improved version of the SL scheme introduced by Skamarock et al. (2008) and based
 202 on the fifth-generation Mesoscale Model (MM5) (Grell et al. 1995).

203 The physics formulation of WRF SL option 1 is based on Monin-Obukhov Similarity
 204 Theory (MOST), and it calculates the friction velocity according to eq.7

$$u_* = \frac{\kappa U}{\log\left(\frac{z}{z_0}\right) - \psi_m\left(\frac{z}{L}\right)}, \quad (7)$$

205 where z is the height, $\kappa = 0.4$ is the von Kármán constant, U is the wind speed at the
 206 lowest computational level, z_0 the roughness length, z/L the stability, and $\psi_{m,h}$ the
 207 integrated Monin-Obukhov similarity function of momentum (or heat) defined according
 208 to eq.8,

$$\psi_{m,h}\left(\frac{z}{L}\right) = \int_0^{z/L} [1 - \phi_{m,h}(\xi)] \frac{d\xi}{\xi}, \quad (8)$$

209 where the dimensionless wind shear ϕ_m and potential temperature gradient ϕ_h are defined
 210 according to eq.9 and eq.10, respectively,

$$\phi_m\left(\frac{z}{L}\right) = \frac{\kappa z}{u_*} \frac{\partial U}{\partial z}, \quad (9)$$

211 and,

$$\phi_h\left(\frac{z}{L}\right) = \frac{\kappa z}{\theta_*} \frac{\partial \theta}{\partial z}, \quad (10)$$

212 with θ_* a temperature scale calculated with eq.11,

$$\theta_* = \frac{\kappa(\theta_a - \theta_g)}{\log\left(\frac{z}{z_0}\right) - \psi_h\left(\frac{z}{L}\right)}, \quad (11)$$

213 where θ_a and θ_g the air and ground surface potential temperature, respectively.
 214

215 In order to use eq.7 in a mesoscale model (i.e., WRF), z_0 is retrieved from the Land Surface
 216 Model (LSM), while the stability z/L is calculated by the SL scheme; and in the case of
 217 WRF SL option 1 with eq.12,

$$\frac{z}{L} = \kappa \frac{g}{\theta_a} z \frac{\theta_*}{u_*^2}. \quad (12)$$

218 For more details on WRF SL option 1, see Jiménez et al. (2012).

219 Alternatively, in this study we implemented Monin – Obukhov (MO) equations to calculate
 220 time series of friction velocity for the period 27 August – 26 September, 2016. This was
 221 preferred over running a complete WRF simulation in view of the difficulty of isolating
 222 the SL scheme from the LSM, and as it reduces uncertainties associated with inaccurate
 223 values of the roughness length, wind speed, and stability parameter, that were passed
 224 directly from the measurements and into the implemented MO equations solved by WRF
 225 SL option 1.

226 The roughness length z_0 was estimated using: (i) The combined wind speed measurements
 227 from the tower and the SODAR at site T1 and (ii) The three instrumented levels at towers
 228 T2 and T6 during periods with westerly winds and Neutral (N) conditions according to the
 229 classical methodology of Panofsky (1962). To reduce uncertainty of z_0 , westerly winds
 230 were defined as being in the segment $270 \pm 5^\circ$. As mentioned, (Sect. 2.3), N conditions
 231 were identified with $|L| > L_{TR}$, with $L_{TR} = 200$. For details on the velocity profiles used in
 232 these calculations, see Fig. A2-4 in Appendix. The roughness length $z_0 = 0.013$ m so
 233 obtained was used to calculate the friction velocity according to eq.13.

$$u_{sim}^* = \frac{\kappa \langle U \rangle}{\log\left(\frac{z}{z_0}\right) - \psi_m\left(\frac{z}{L}\right)}. \quad (13)$$

234 Considering that many high-resolution simulations have grid-sizes $\sim 1-3$ km (Hong and
 235 Dudhia 2012), tests were conducted on the ability of the selected SL scheme to capture a

236 friction velocity that agrees with the observed spatially averaged friction velocity. The
 237 friction velocity at $z = 10$ m was simulated, considering that all towers had instruments at
 238 that height and that the first level of NWP models is typically set to 10 m.
 239 Given the dependence of u_* on the local wind speed and stability (Eq. 7), these variables
 240 were spatially averaged for $z = 10$ m at all sites, as indicated by the brackets in Eq. 13.

241 3 Results

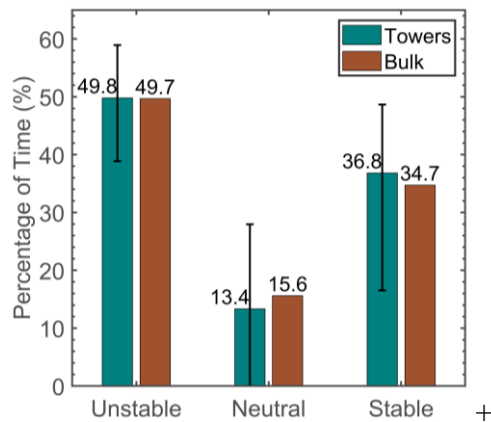
242

243 3.1 Stability Regimes

244

245 Typical ASL parameterizations diagnose the friction velocity and temperature fluxes in
 246 terms of the stability parameter z/L , but in reality, the latter is variable within a grid cell.
 247 To illustrate this variability, for the Aug 27 to Sep 26 period, we calculated the percentage
 248 of time the stability regimes Unstable (UN), Neutral (N), and Stable (S) occurred at each
 249 tower location. For each stability regime, the results were averaged across all towers, and
 250 consistent with Sect. 2.3, only periods with wind direction in the [westerly] sector 240° -
 251 290° are considered here and in Sect. 3.2 and Sect. 3.3.

252 As shown in Fig. 4, the UN, N, and S stability regimes were observed approximately 49
 253 (49), 13 (15), and 37 (35) percent of the time, respectively. The parenthetical values are the
 254 percentages evaluated with the bulk Obukhov length (L_{bulk}) described in Sect. 2.3. The
 255 higher number of UN cases (49%) compared to S ones (37%) is due to the fact that winds
 256 in the sector 240° - 290° are more frequently observed during daytime conditions for this
 257 season of the year.



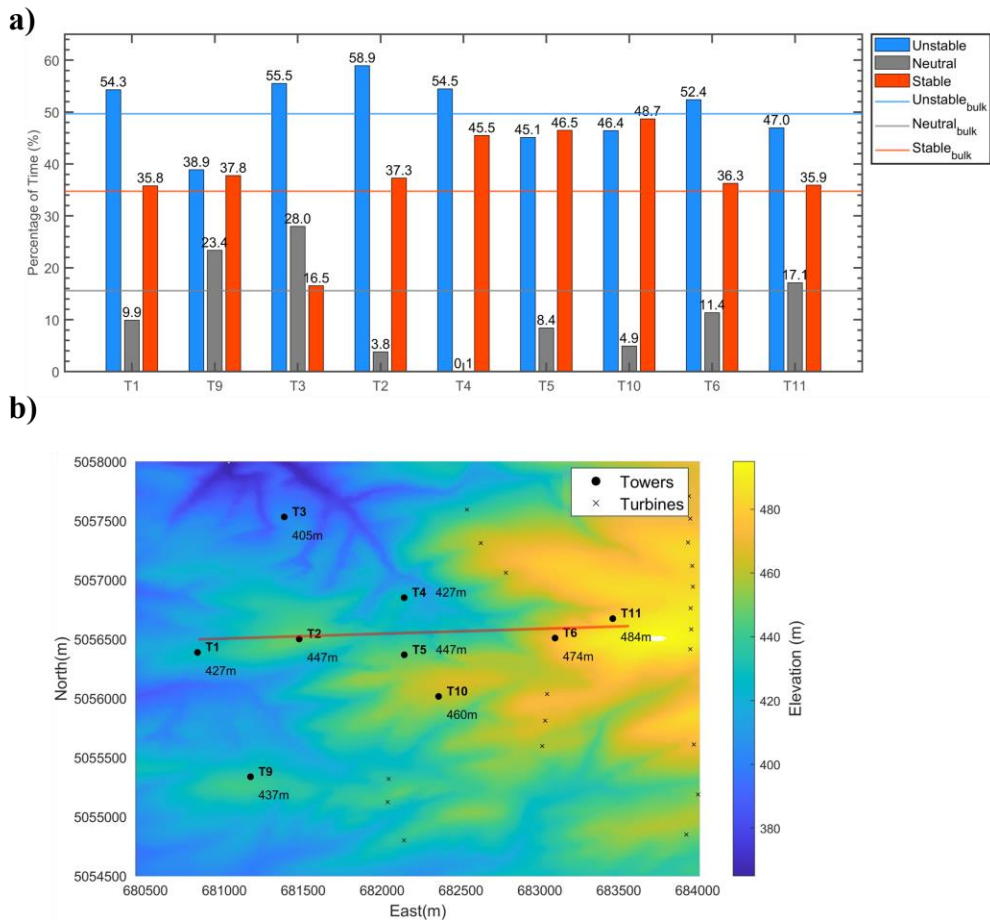
258

259 Figure 4: Percentage of time the stability regimes UN , N , and S were present during Aug 27 to Sep 26.
 260 Calculations were made for each tower, and the average across all towers is shown by teal-blue bar with the
 261 error bar indicating the maximum and minimum values. The brown bar corresponds to the distribution of
 262 stability regimes calculated using the ‘Bulk Obukhov length’ L_{bulk} (Sec. 2.3).

263

264 The good agreement between the green and the brown bars in Fig. 4 suggests the overall
 265 stability of the instrumented region can be characterized with either $\langle L \rangle$ or L_{bulk} . The error
 266 bars in Fig. 4 are associated with the spatially averaged stability (green bars), and for each
 267 stability regime (UN, N and S), they indicate the maximum and minimum percentage of
 268 the time the same stability was observed at any of the towers.

269 To further interpret these results, Fig. 5a shows the percentage of time each stability regime
 270 was reported for all tower locations, where the blue, grey, and orange horizontal lines
 271 correspond to the percentage of time the UN, N, and S regimes assessed with L_{bulk} were
 272 reported, respectively. The tower locations and terrain elevations corresponding with the
 273 data plotted in Fig. 5a are shown in Fig. 5b.



274
 275 Figure 5: (a) Percentage of time stability regimes were present at each tower location (T1 to T9) during Aug
 276 27 to Sep 26. The color bar representation is in the inset. The horizontal lines of the same colors correspond
 277 to that based on *Bulk Obukhov length* for the same stability regimes. (b) Topography of instrumented region
 278 and tower's locations (same as Fig. 1).
 279

280 The higher spatial variability reported for the stable regime and indicated by the error bars
 281 in Fig. 4 was affected by the smaller number of stable cases at site T3. This site had an
 282 elevation of 405 m and it was located about 1 km north from site T2 (see Fig. 5b). At site
 283 T3, winds in the sector 240°-290° were less frequent than at other locations, and when they

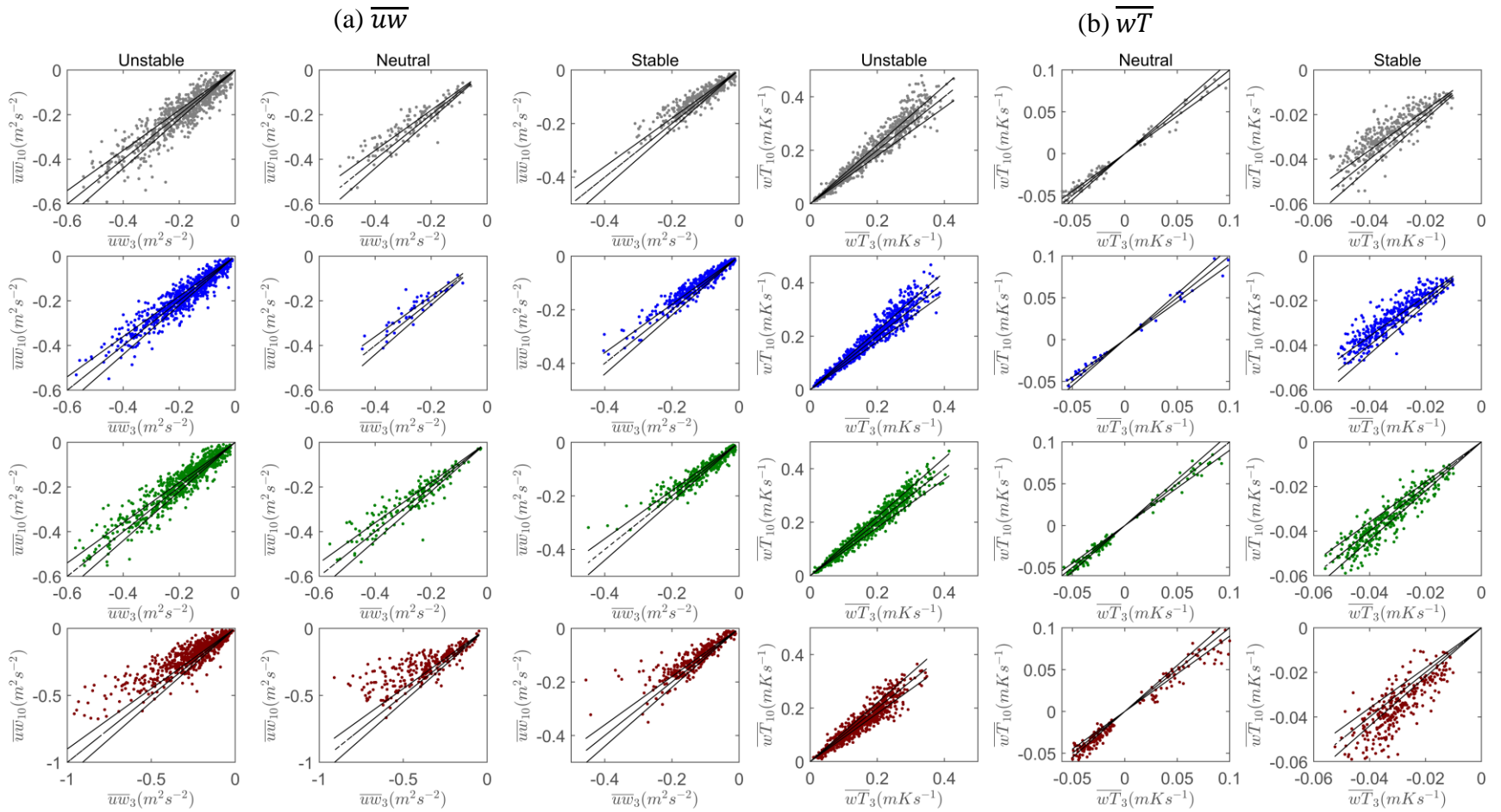
284 occurred, they were associated with higher values of friction velocity. In addition, at this
285 site the range of variability for the Obukhov length was bigger than for the rest of the
286 towers (-400 m to 400 m), and several cases with values of $L^* > 0$ fell in the neutral regime.
287 On the other hand, the north-south transect of towers between sites T4, T5, and T10, and
288 associated with terrain elevations of 427 m, 447 m, and 460 m, respectively, exhibited a
289 higher number of stable cases. With regards to diagnosing stability in heterogeneous
290 terrain, no clear correlation between the stability regimes and elevation was found.
291 Given the dependence of the Obukhov length on the friction velocity and temperature
292 fluxes, we studied their spatial variability in Sect. 3.2 and Sect. 3.3.

293 **3.2 Constant-Flux Layer**

294
295 As mentioned in Sect.1, the existence of a Constant-Flux Layer (CFL) is key to the SL
296 parameterizations of NWP models. In this section, we used towers T1, T2, T6, and T11
297 (horizontal line in Fig. 5b) to study the CFL concept as a function of i) stability regime, ii)
298 flux magnitude, and iii) tower location. For doing so, the differences between $\overline{u'w'}$ and
299 $\overline{w'T'}$ at $z = 3$ m and those at $z = 10$ m were calculated individually for T1, T2, T6, and
300 T11. In this study, because of the small separation between levels (i.e., 7m), the CFL
301 approximation was taken to be valid when the differences between these two levels were
302 less than 10%. Consistent with the study of Sfyri et al. (2018), momentum and temperature
303 fluxes with absolute values smaller than $0.01 \text{ m}^2 \text{ s}^{-2}$ and 0.01 K m s^{-1} , respectively, were
304 not included in the CFL analysis, as they are characterized by large random errors and
305 affected by mesoscale trends (Sfyri et al., 2018; Klipp and Mahrt, 2004).

306 To study the vertical variability of fluxes, values of $\overline{u'w'}$ at $z = 3$ m are plotted against
307 those at $z = 10$ m in Fig. 6a. Similarly, values of $\overline{w'T'}$ at $z = 3$ m are plotted against those
308 at $z = 10$ m in Fig. 6b. These plots were calculated for all tower sites (T1, T2, T6, and T11)
309 and for each stability regime (UN, N, and S). On Figs. 6 a-b, lines with slopes 1, 0.9, and
310 1.1 are plotted, and all points located in the area bounded by slope = 0.9 and 1.1 lines were
311 assumed to satisfy the CFL approximation.

312



313 Figure 6: (a) Scatter plots of longitudinal momentum flux ($\overline{u'w'}$) at $z = 3$ m (x-axis) versus longitudinal momentum flux ($\overline{u'w'}$) at $z = 10$ m (y-axis); (b) Same as
 314 in (a) but for the temperature flux ($\overline{w'T'}$). The columns correspond to Very Unstable, Near Neutral, and Very Stable regimes (from left to right), and the rows to
 315 towers T1 (gray), T2 (blue), T6 (green), and T11 (maroon).

316 3.2.1 Fluxes Vertical Variability

317

318 ▪ Longitudinal Momentum Flux ($\overline{u'w'}$)

319 As seen in Fig. 6a, the differences in the longitudinal momentum flux ($\overline{u'w'}$) were more
320 affected by the stability regimes (UN, N, or S) than by the towers' locations, except for site
321 T11, where the differences between levels and the scatter in the data were the highest of
322 all sites. In general, for the UN regime, $\overline{u'w'}$ varied in the interval $[-0.6, 0] \text{ m}^2 \text{ s}^{-2}$, the
323 median $\overline{u'w'}$ was about $-0.2 \text{ m}^2 \text{ s}^{-2}$. In addition, a bigger range of variability was reported
324 at site T11, where the values of $\overline{u'w'}$ at $z = 3\text{m}$ were systematically higher than 10 % of
325 those at $z = 10\text{m}$, e.g., see the high number of points above slope = 0.9 line in Fig. 6a.

326 As discussed earlier, neutral conditions (as defined in Table 2) were infrequently reported,
327 and at sites T1, T2, T6, and T11, they were only present ~ 5-17% of the time (see Fig. 5a).
328 For the N regime, $\overline{u'w'}$ varied between $[-0.5, -0.1] \text{ m}^2 \text{ s}^{-2}$, the median $\overline{u'w'}$ was about -0.3
329 $\text{m}^2 \text{ s}^{-2}$, and most measurements were associated with values of $L^* < 0$. The scatter of the
330 data as well as the differences between levels were smaller than for the UN regime, likely
331 due to the higher signal-to-noise ratio in $\overline{u'w'}$ measurements during high wind speed
332 periods. For the S regime, $\overline{u'w'}$ varied in the interval $[-0.4, 0] \text{ m}^2 \text{ s}^{-2}$, and the median $\overline{u'w'}$
333 was about $-0.1 \text{ m}^2 \text{ s}^{-2}$. For this regime, the scatter of $\overline{u'w'}$ between levels was smaller than
334 for the UN regime, which was expected locally, as wind speed and flux magnitude tend to
335 be smaller for stable periods (Stull, 1988; Pope 2000). On the other hand, we expected to
336 find smaller differences between sites for the UN regime, as the role of terrain
337 heterogeneities should have been attenuated by the bigger eddy size and enhanced mixing
338 during convective conditions, however, percentual differences between sites were
339 comparable between the UN and S regimes.

340 ▪ Temperature Flux ($\overline{w'T'}$)

341 The variability of $\overline{w'T'}$ was also more affected by the stability regimes (UN, N, or S) than
342 by the towers' locations. For the UN regime, the temperature flux ($\overline{w'T'}$) varied in the
343 interval $[0, 0.4] \text{ K m s}^{-1}$, and the median $\overline{w'T'}$ was about 0.16 K m s^{-1} . In addition, $\overline{w'T'}$
344 measurements were symmetrically distributed with respect to slope = 1 lines, and the
345 differences between levels and scatter in the data were smaller than for $\overline{u'w'}$, nonetheless,
346 as we expected, the variability of the temperature flux was more complex than for the
347 momentum flux. For the N regime, a narrow range of variability for $\overline{w'T'}$ between $[-0.05,$
348 $0.1] \text{ K m s}^{-1}$ was observed for all the sites. Moreover, the scatter between levels was the
349 smallest of all stability regimes. Nonetheless, a high number of points did not satisfy the
350 CFL, likely due to the small magnitude of the fluxes, and also a higher number of points
351 did not satisfy our quality control requirements when compared with the momentum flux
352 ($\overline{u'w'}$), i.e., the absolute values of $\overline{w'T'}$ were $< 0.01 \text{ K m s}^{-1}$, and/or the fluxes at levels z
353 = 3m and $z = 10\text{m}$ exhibited different signs. For the S regime, $\overline{w'T'}$ varied in the interval

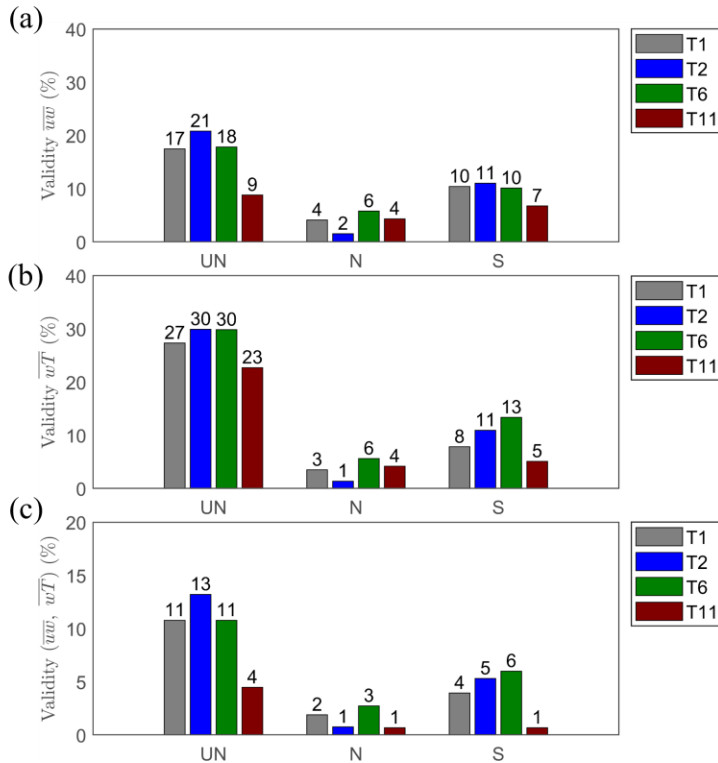
354 $[-0.05, 0] \text{ K m s}^{-1}$, and both the scatter between levels and the differences between sites
355 were higher than for the UN regime. For example, for the westernmost sites, i.e., T1 and
356 T2, values of $\overline{w'T'}$ at $z = 10\text{m}$ were systematically lower than those at $z = 3\text{m}$. e.g., see
357 how the distribution of points is skewed with respect to slope = 1 lines in Fig. 6b. On the
358 other hand, at sites T6 and T11, located about 1.6 and 2 kilometres east from site T2,
359 respectively, the terrain elevation was $\sim 30\text{-}40$ meters higher than at T2, and $\overline{w'T'}$ values
360 at $z = 10 \text{ m}$ were frequently higher than those at $z = 3\text{m}$, especially at site T11. Site T11
361 was located $\sim 200\text{m}$ north from the transect between towers T1, T2, and T6, and local
362 heterogeneities and enhanced surface roughness due to the presence of wheat crops could
363 have affected the measurements.

364 **3.2.2 Constant-Flux Layer Validity**

365
366 Because the number of UN, N, and S cases were not constant across sites (as shown in Fig.
367 5a), for each tower site (T1, T2, T6, and T11) and stability regime (UN, N, and S), the CFL
368 validity was calculated as the ratio between the total number of points located in the area
369 bounded by slopes = 1.1 and 0.9 lines in Figs. 6a-b (for the momentum ($\overline{u'w'}$) and
370 temperature ($\overline{w'T'}$) flux, respectively), and the total number of records (addition of UN,
371 N, and S cases), where the latter was the same for all towers and corresponded to the total
372 number of westerly records discussed in Sect. 3.1.

373 The CFL validity results (expressed in % of time) for the momentum flux ($\overline{u'w'}$), the
374 temperature flux ($\overline{w'T'}$), and both momentum and temperature fluxes ($\overline{u'w'}$ and $\overline{w'T'}$)
375 simultaneously are shown in Figs. 7a-c, respectively.

376 The CFL validity for $\overline{u'w'}$ and $\overline{w'T'}$ was higher for the UN regime. Nonetheless, the CFL
377 validity for $\overline{u'w'}$ was only $\sim 20\%$ at T1, T2, and T6, and $\sim 10\%$ at T11. While the CFL
378 validity for $\overline{w'T'}$ was only $\sim 30\%$ at T1, T2, and T6, and $\sim 10\%$ at T11. For the S regime,
379 the CFL validity for $\overline{u'w'}$ was $\sim 10\%$, while the CFL validity for $\overline{w'T'}$ exhibited slightly
380 higher variability across the sites, i.e., between 8-13% at T1, T2, and T6, and 5% at T11.
381 For the N regime, the CFL was satisfied between 1-6 % of the time, so no important
382 differences between towers were observed. Note that this regime was highly infrequent
383 compared to the UN or the S regime. For completeness, as indicated in Fig. 7c, the
384 percentage of cases that simultaneously satisfied the CFL for $\overline{u'w'}$ and $\overline{w'T'}$ were $< 10\%$
385 for the UN regime, $< 3\%$ for the N regime, and between 1-6% for the S regime. Thus, the
386 data suggests the CFL generally does not hold, not even at small horizontal and vertical
387 scales such as the ones explored in this experiment.



388

389 Figure 7: (a) CFL Validity (in % of time) for the momentum flux $\overline{u'w'}$, (b) temperature flux $\overline{w'T'}$, and (c)
 390 momentum and temperature flux simultaneously ($\overline{u'w'}$, $\overline{w'T'}$). The results were calculated for each stability
 391 regime (UN, N, and S), and for each tower location (T1, T2, T6, and T11).

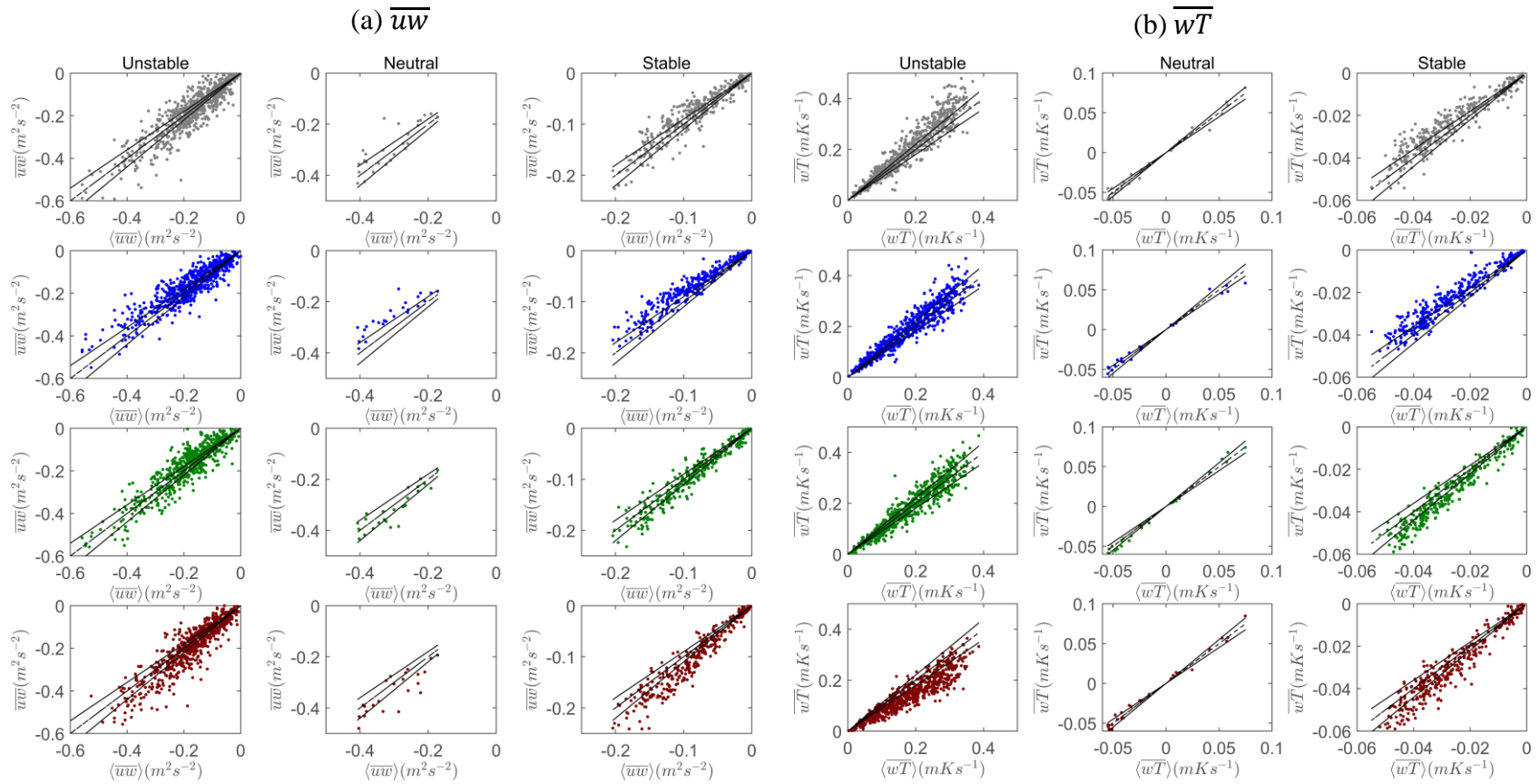
392

393 3.3 Fluxes Horizontal Variability

394

395 To study the horizontal variability of fluxes, local values of $\overline{u'w'}$ are plotted against $\langle \overline{u'w'} \rangle$
 396 (spatial-averaging across towers T1, T2, T6, and T11) in Fig. 8a. Similarly, $\overline{w'T'}$ from the
 397 tower sites against $\langle \overline{w'T'} \rangle$ are shown in Fig. 8b. The plots were done for each stability
 398 regime (UN, N, and S), and they seek to quantify differences between local turbulent fluxes
 399 and their spatially averaged counterparts.

400 As in Sect. 3.2, on Figs. 8a-b, lines with slopes 1, 0.9, and 1.1 are plotted. The results were
 401 similar to the ones associated with the CFL in Sect. 3.2.



402 Figure 8: (a) Scatter plots of $\overline{u'w'}$ at $z = 10$ m (y-axis) versus its spatially averaged value $\langle \overline{u'w'} \rangle$ at the same height (x-axis) at a given time;
 403 but for $\overline{w'T'}$ at $z = 10$ m (y-axis). The columns correspond to VU, NN, and VS (from left to right), and the rows to towers T1 (gray), T2 (blue), T6 (green), and
 404 T11 (maroon).

405

406 ▪ Unstable (UN)

407 This regime exhibited the highest deviations between the local and spatially averaged
408 momentum flux, $\overline{u'w'}$ and $\langle u'w' \rangle$, respectively. At all sites, deviations $> 10\%$ were
409 observed. At T1, T2, and T6, data points were symmetrically distributed with respect to
410 slope = 1 lines (Fig. 8a). In contrast, at T11, values of $\overline{u'w'}$ were higher than $\langle u'w' \rangle$ most
411 of the time. For this stability, the similarity between the horizontal variability of $\overline{u'w'}$ and
412 the CFL efficacy of the latter is remarkable.

413 On the other hand, this regime also exhibited the highest deviations between the local and
414 spatially averaged temperature flux, $\overline{w'T'}$ and $\langle w'T' \rangle$, respectively. At all sites, deviations
415 $> 10\%$ were frequently observed. At all sites (except for T11), data points were
416 symmetrically distributed with respect to slope = 1 lines (Fig. 8b) and the horizontal
417 variability of $\overline{w'T'}$ was less than for $\overline{u'w'}$ for this stability, analogous to the CFL results
418 for $\overline{w'T'}$ in Sect. 3.2.

419 ▪ Neutral (N)

420 For all sites, deviations between the local and spatially averaged momentum flux were $<$
421 10% most of the time, and the horizontal variability of $\overline{u'w'}$ was the lowest of all stability
422 regimes. Nonetheless, the distribution of points with respect to slope = 1 lines presented
423 more site-to-site variability when compared to the CFL results of Sect. 3.2 ($\overline{u'w'}$ - N), i.e.
424 values of $\overline{u'w'}$ at T2 had less scatter than other sites and were systematically lower than
425 the spatially averaged flux $\langle u'w' \rangle$. At T11, differences between local and spatially
426 averaged values at $z = 10$ m were about the same of those observed at T1, T2, and T6 (as
427 opposed to the CFL results reported in Sect. 3.2). This suggests that the least agreement
428 with the CFL concept for N conditions at T11 was a result of anomalously high values of
429 $\overline{u'w'}$ at $z = 3$ m (Fig. 5a). Nonetheless, it is important to notice that the number of N points
430 were lesser than in Sect. 3.2, a consequence of requiring N conditions to be simultaneously
431 satisfied at sites T1, T2, T6, and T11.

432 On the other hand, for all sites, deviations between the local and spatially averaged
433 temperature flux were $< 10\%$ most of the time, and the scatter of the data for $\overline{w'T'}$ was
434 less than for $\overline{u'w'}$ during N conditions (Fig. 8a-b). These results were analogous to the ones
435 in Sect. 3.2 ($\overline{w'T'}$ -N).

436 ▪ Stable (S)

437 The scatter between local and spatially averaged momentum flux was lower than for the
438 UN regime, and the differences between sites more evident. This is analogous to what we
439 observed in Sect. 3.2 ($\overline{u'w'}$ - S). For this regime, $\overline{u'w'}$ differences between sites were
440 higher than the differences between levels (for fixed sites), as evidenced by the different
441 distributions of points with respect to slope =1 lines for sites T1, T2, T6, and T11 shown
442 in Fig. 8a. More interestingly, the magnitude of the flux did not affect the differences

443 between local values of $\overline{u'w'}$ and the spatially averaged flux $\langle \overline{u'w'} \rangle$, which was analogous
 444 to what we observed for the CFL results in Sect. 3.2 ($\overline{u'w'} - S$)
 445 On the other hand, the scatter between the local and spatially averaged temperature flux
 446 was lower than for the UN regime, and deviations higher than 10% were frequently
 447 observed at all sites. In addition, the differences between sites were the highest of all
 448 stability regimes, similarly to what we observed for $\overline{u'w'}$.
 449

450 **3.4 Surface-Layer Parameterizations**

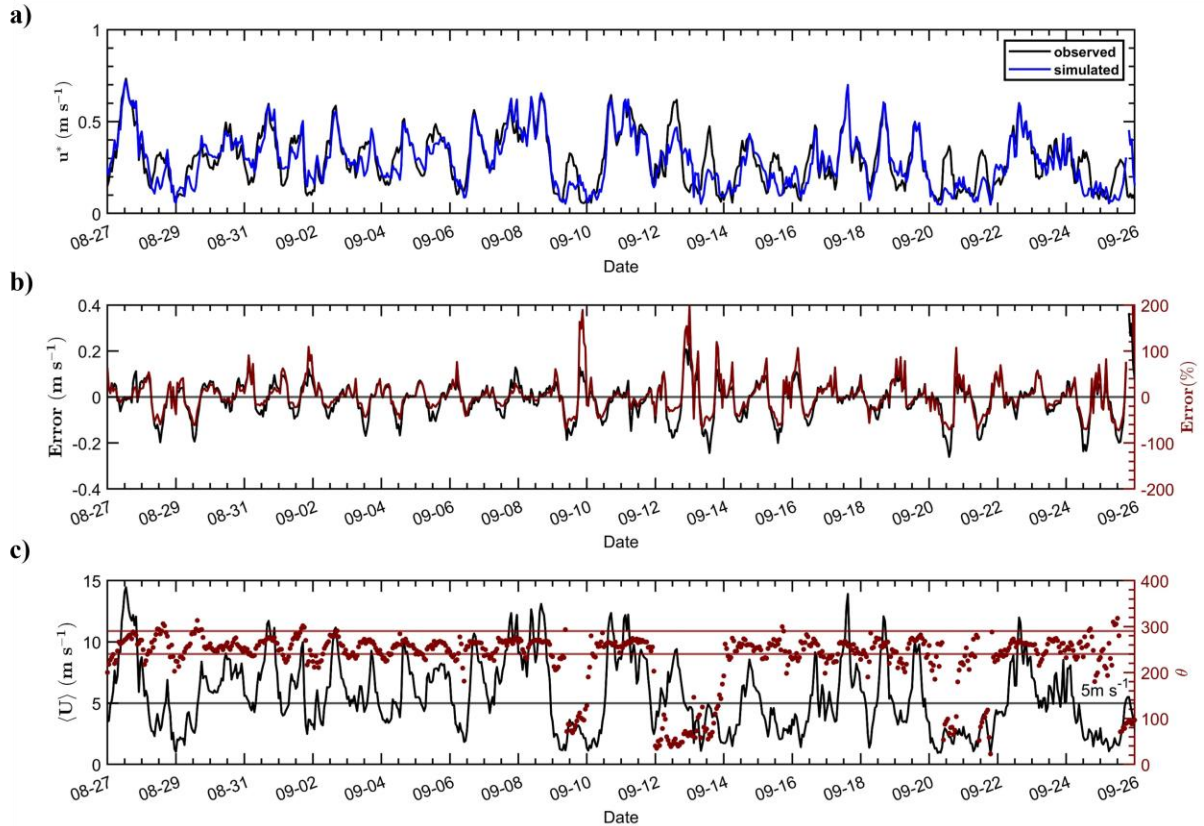
451
 452 We calculated time series of the simulated and observed (spatially averaged across all 9
 453 towers) friction velocity for the period 27 August – 26 September, 2016. The time series
 454 of simulated (blue) and observed (black) friction velocity are shown in Fig. 8a, and the
 455 difference between them is the error calculated according to eq.14 and indicated in Fig. 8b
 456 (left y axis).

$$Error (m s^{-1}) = u_{sim}^* - \langle u^* \rangle, \quad (14)$$

457 with u_{sim}^* and $\langle u^* \rangle$, the simulated and spatially averaged observed friction velocity
 458 described in Sect. 2.4 and calculated with eq.13 and eq.6, respectively. The error (eq.14)
 459 expressed as a percentage of the observed friction velocity is the percentual error calculated
 460 with eq.15 and indicated in Fig. 8b (right y axis).

$$Error (\%) = \frac{Error}{\langle u^* \rangle} \cdot 100 \quad (15)$$

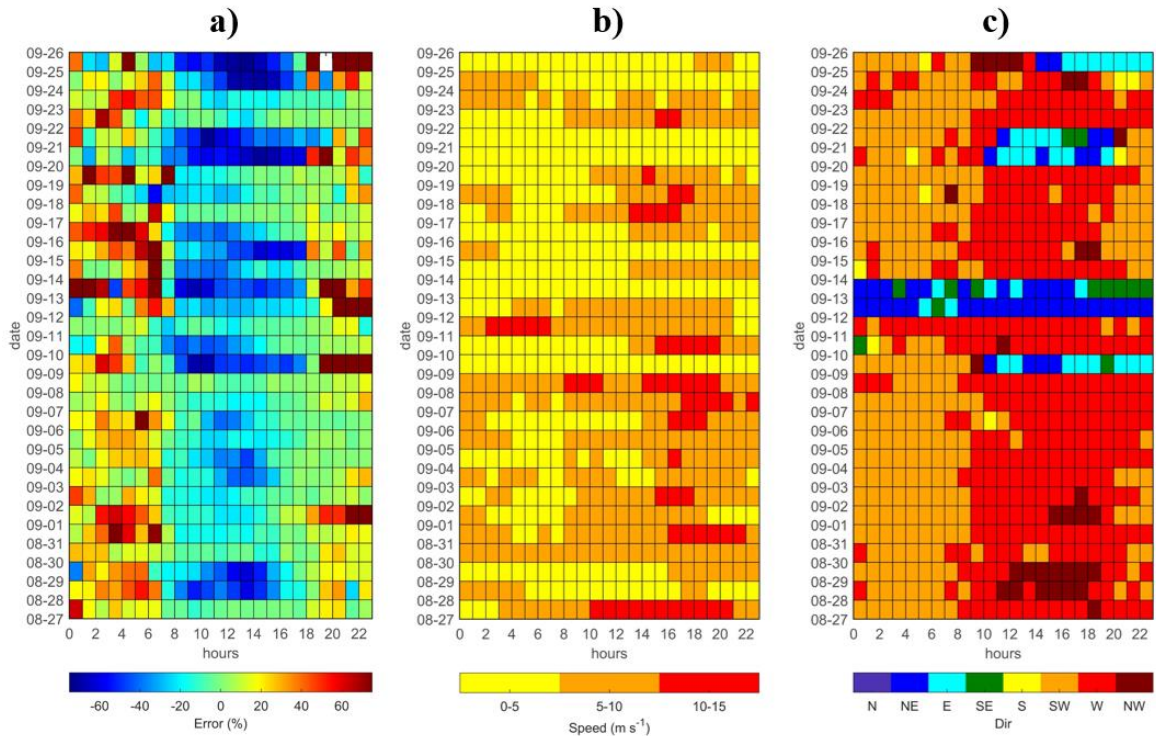
461



462

463 Figure 9: (a) Time series of friction velocity for 27 August – 26 September 2016. The black line is the
 464 spatially averaged friction velocity $\langle u^* \rangle$ measured by all towers at $z = 10 \text{ m}$, and the simulated friction
 465 velocity at $z = 10 \text{ m}$ is in blue; (b) Time series of the Error between the two-time series of (a) in m s^{-1} (left y
 466 axis) and in percentage (right y axis); (c) Time series of the observed spatially-averaged wind speed (black line)
 467 and wind direction (maroon line) with the black line indicating the 5 m s^{-1} threshold and the maroon lines
 468 demarcating the westerly wind regime between 240° - 290° .
 469

470 To effectively study the skill of the SL scheme for the period between 27 August – 26
 471 September 2016, the data plotted in Figs. 9b-c were used to calculate error, wind speed,
 472 and wind direction colormaps, as shown in Figs. 10a-c, respectively. In Figs. 10a-c, the
 473 rows corresponds to different days, while the columns corresponds to different hours (in
 474 Pacific Standard Time). Since the relationship between the skill of the SL scheme and the
 475 current meteorological conditions was of interest, we adopted the wind-regime
 476 classification used by Fernando et al. (2015) for their complex terrain observations:
 477 Quiescent (wind speeds between 0 - 5 m s^{-1}), *Transitional* (wind speeds between 5 - 10 m s^{-1}),
 478 and *Synoptic* (wind speeds higher than 10 m s^{-1}), with the difference being that we used
 479 the observed winds at $z = 10 \text{ m}$ instead of the 700 -hPa winds. In this classification,
 480 *Transitional* flows are associated with rapidly changing winds and turbulence levels, such
 481 as the ones observed during the morning and evening transition periods, while *Synoptic*
 482 flows are associated with synoptic winds higher than 10 m s^{-1} (Fernando, 2010).



483

484 Figure 10: Color maps of (a) 1h Error (%) between simulated and observed friction velocities; (b) 1h wind
 485 speed regimes; and (c) 1h wind direction regime for the period 27 August 2016 to 26 September 2016. The
 486 abscissa indicates the local time whereas the ordinate is the date.
 487

488 As shown in Fig. 9b, errors between -0.1 to 0.1 m s^{-1} were observed most of the time, which
 489 when normalized by the observed friction velocity, corresponds to -40 to 85% errors. The
 490 friction velocity was frequently underpredicted by the SL scheme during the day and
 491 overpredicted at night, when high percentual errors were reported (see Figs. 9a-b). For the
 492 nominally observed westerly winds (maroon lines in Fig. 9c) with speeds $> 5 \text{ m s}^{-1}$ (black
 493 horizontal line in Fig. 9c), the implemented SL scheme captured the diurnal variability of
 494 friction velocity well (Figs. 9a-b).

495 For example, on 27 August, westerly winds $> 5 \text{ m s}^{-1}$ were present most of the day, and the
 496 simulated friction velocity was almost identical to the observations between 07:00-16:00
 497 LT (local time) (Fig. 9a; Fig. 10a-c). For this day, the Mean Absolute Error (MAE) was
 498 about 9% of the observed friction velocity (daily averaged). Similar cases were observed
 499 on 06, 17, and 19 September, all associated with westerly winds with speeds $> 5 \text{ m s}^{-1}$ and
 500 MAEs between 8-16% of the observed friction velocity (Fig. 9c; Fig. 10b, c).

501 For the rest of the days, the SL scheme was able to capture the time variability trend of
 502 friction velocity over a diurnal cycle, but not the exact value. This was expected given the
 503 heterogeneous nature of the terrain and the wide range of meteorological phenomena that
 504 characterizes the region (Wilczak et al. 2019). In fact, errors as high as 60% of the observed

505 friction velocity were present on most days at night when the friction velocity was less than
 506 about 0.2 m s^{-1} (for more details see Fig. A5).

507 The study period spanned diverse meteorological regimes. For instance, cases with
 508 predominantly westerly winds with both quiescent and transitional regimes were observed
 509 (i.e. 03, 04 September). For the rest of the westerly-flow days, particularly during quiescent
 510 winds, the flow exhibited a characteristic diurnal variability with a northerly/northwesterly
 511 component (NW) during daytime and a southerly/southwesterly component (SW) during
 512 nighttime (e.g., 28, 29 August and 24 September).

513 Cases with easterly winds with quiescent and transitional regimes were also observed, but
 514 they were not analyzed as they might be contaminated by wake effects of an array of
 515 turbines located east of the towers (Fig. 1a). Also recall that the roughness length used in
 516 simulations ($z_0 = 0.013 \text{ m}$) corresponded to westerly winds.

517 The degree of subgrid variability associated with the observed errors at NWP-model
 518 resolution for selected days was also investigated. The subgrid variability was assessed
 519 through the Mean Absolute Deviation (MAD) calculated according to eq.16.

$$MAD = \frac{1}{N} \sum_{i=1}^N |u_{obs}^*(x_i, t) - \langle u_{obs}^* \rangle| \quad (16)$$

520 A high temporal correlation between the Error and the spatial heterogeneity of the flow,
 521 quantified through the Mean Absolute Deviation (MAD), was noted, as discussed below.

522 From all westerly-flow days in the period Aug 27 – September 26, 2016, we identified the
 523 ones associated with the highest and the lowest SL scheme errors, which are indicated in
 524 Tables 3- 4, respectively. These errors were quantified by the MAE, calculated for i) A 24-
 525 hour period (denoted by MAE_{day} in Tables 3-4), and ii) between 12:00-14:00 LT (denoted
 526 by MAE_{sub} in Tables 3-4). (MAE_{day}) and (MAE_{sub}) expressed as a percentage of the
 527 temporally averaged observed friction velocity are denoted by $Error_{day}$ and $Error_{sub}$ in
 528 Tables 3-4.

529 Table 3: Days associated with the highest SL scheme errors for 27 August 2016 to 26 September 2016. The
 530 Mean Absolute Error (MAE) and the percentual error (Error) were calculated daily (MAE_{day} and $Error_{day}$)
 531 and between 12:00 –14:00 LT (MAE_{sub} and $Error_{sub}$). These metrics and their associated wind regimes are
 532 indicated for the list of days shown below.

Date	MAE_{day} (m s ⁻¹)	$Error_{day}$ (%)	MAE_{sub} (m s ⁻¹)	$Error_{sub}$ (%)	Wind Dir.	Speed Range (m s ⁻¹)	Wind Regime
08/28/16	0.08	32.8	0.17	52.7	NW	5-10	Q, T
08/29/16	0.06	26.6	0.18	57.3	NW	<5	Q
09/03/16	0.05	17.6	0.15	40.7	W	5-10	Q, T
09/04/16	0.04	14	0.13	38.1	W	5-10	Q, T
09/15/16	0.08	38	0.16	52	W	<5	Q
09/24/16	0.08	35.4	0.23	69.9	W, SW	<5	Q

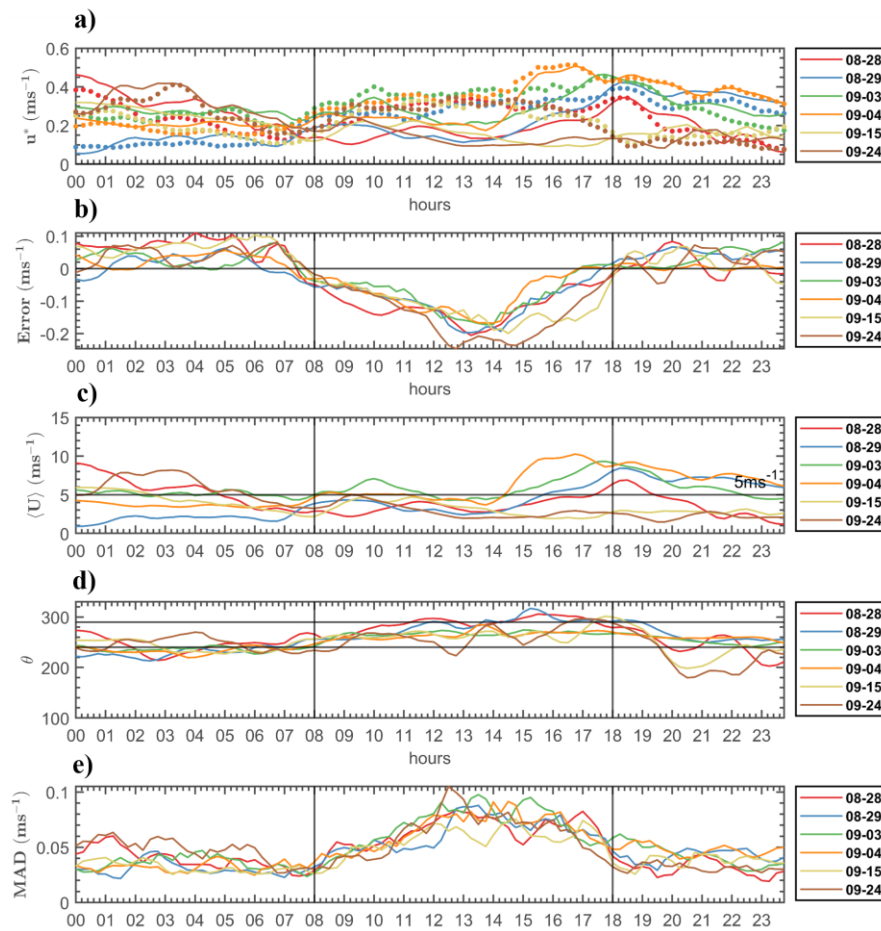
533

534 Table 4: Analogous to Table 3, but for selected days with the lowest SL scheme errors for 27 August 2016
 535 to 26 September 2016.

Date	MAE _{day} (m s ⁻¹)	Error _{day} (%)	MAE _{sub} (m s ⁻¹)	Error _{sub} (%)	Wind Dir.	Speed Range (m s ⁻¹)	Wind Regime
08/27/16	0.04	8.5	0.01	1.1	W	5-15	T
09/06/16	0.04	12.6	0.07	24.9	W	2-11	Q, T
09/17/16	0.03	8	0.01	1	W	4-15	Q, T
09/19/16	0.04	15.5	0.02	5.1	W	4-10	Q, T

536

537 For the list of days in Table 3 (associated with the poorest performance of the SL scheme),
 538 positive errors of about 0.1 m s⁻¹ were frequently observed at night, while variable negative
 539 errors as high as 0.2 m s⁻¹ were observed during the day (Fig. 11a-b). The impact of these
 540 errors on the skill of the SL scheme depends on the magnitude of the friction velocity. For
 541 instance, 1-hour (positive) and (negative) errors between (30-106%) and of about (60%) of
 542 the observed friction velocity were reported.



543

544 Figure 11: 24-hour time series of (a) Observed (dots) and simulated (solid lines) friction velocity; (b) Error;
 545 (c) Observed wind speed; (d) Wind direction (θ); and (e) Mean Absolute Deviation (MAD) of friction
 546 velocity at $z = 10$ m calculated using all the towers. The selected days 08/28/16, 08/29/16, 09/03/16, 09/04/16,

547 09/15/16, and 09/24/16 are indicated by different colors. The abscissa in (a)-(e) is the hour of the day in local
548 time.

549

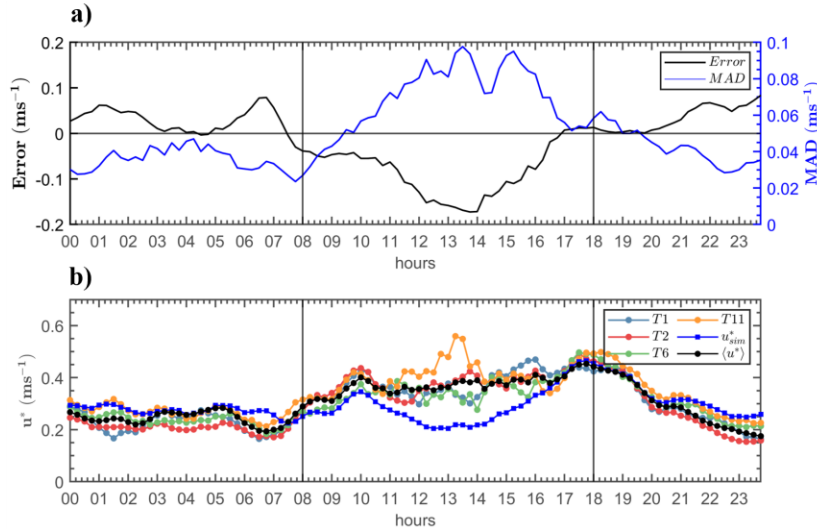
550 For the six cases in Table 3: 28, 29 August, and 03, 04, 15, and 24 September, the
551 parameterization scheme was challenged during 08:00-18:00 LT (Fig. 11a-b), and the
552 winds were approximately westerly, as indicated by the two horizontal lines in Fig. 11d.

553 The error defined in eq.14 increased monotonically (in magnitude) between 08:00 LT until
554 about 12:00-14:00 LT when it peaked, and it decreased monotonically until 18:00 LT (Fig.
555 11b). For all days, the highest errors were associated with quiescent winds between 08:00-
556 14:00 LT. However, on 28, 29 August and 3, 4 September, the errors between 14:00-18:00
557 LT were smaller than the errors on 15, 24 September, likely in part due to the presence of
558 transitional winds for the latter days (between 5-10 m s⁻¹) (Fig. 11c).

559 As indicated in Table 3, the Mean Absolute Error (MAE) between 12:00-14:00 LT (when
560 errors peaked) (MAE_{sub}) was about an order of magnitude higher than the daily MAE
561 (MAE_{day}). Values of (MAE_{day}) and (MAE_{sub}) expressed as a percentage of the observed
562 friction velocity are denoted by (Error_{day}) and (Error_{sub}) in Table 3, respectively. Error_{day}
563 varied between 18-38%, while Error_{sub} varied between 38-70%. In general, the percentual
564 error between 12:00-14:00 LT (Error_{sub}) was approximately twice the daily percentual error
565 (Error_{day}), thus suggesting the skill of SL schemes in complex terrain is more sensitive to
566 prediction errors during the day (as previously observed in Fig. 11a).

567 As shown in Fig. 11e, for all selected days, the MAD followed the simulation error between
568 08:00-18:00 LT (Fig. 11b), suggesting that subgrid variability might be a good predictor
569 for errors when 1 - 3 km horizontal resolution is used for the NWP model in point.

570 Further, the time evolution of the error and MAD over the diurnal cycle for 03 September
571 shown in Fig. 12a suggests that during 08:00-18:00 LT, the Error and MAD peaked around
572 12:00-14:00 LT, consistent with previous observations (Fig. 11a), and the SL scheme
573 under-predicted the spatially averaged friction velocity. Moreover, the parameterization
574 scheme under-predicted the observed friction velocity at T1, T2, T6, and T11 (east-west
575 transect) and deviated from the spatially averaged friction velocity (Fig. 12b), consistent
576 with the increasing trend of MAD.

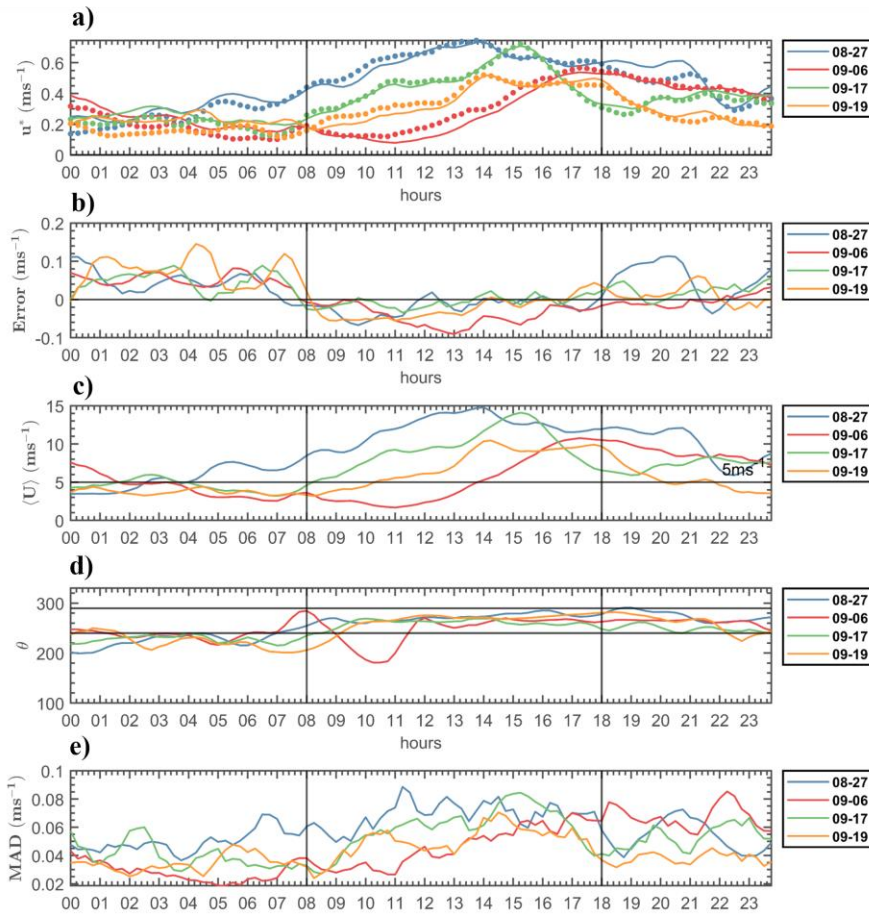


577
578
579
580
581
582
583

Figure 12: 24-hour time-series for 03 September 2016. (a) Error (black line with values on the left ordinate) and MAD (blue line, right ordinate); and (b) Observed friction velocity at T1, T2, T6 and T11 compared with the spatially averaged observed $\langle u^* \rangle$ (blue line with markers) and simulated friction velocity u^* (black line with markers). The abscissa in (a)-(b) is the hour of the day in local time.

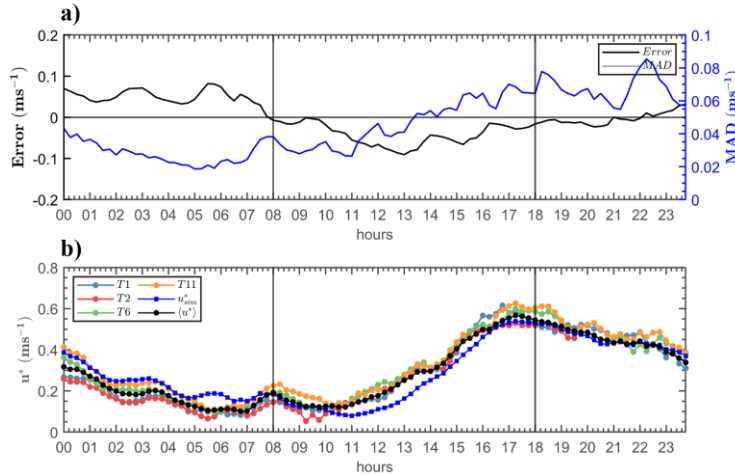
584 For completeness, the time series in Fig. 11a-e were recalculated for the days in Table 4
585 and are shown in Fig. 13a-e. These days had the lowest errors for the entire observational
586 period, as signified by $\text{Error}_{\text{day}}$ between 8-16% in Table 4. In contrast to what we observed
587 for the list of days in Table 3 (Fig. 11a), the simulated friction velocity was remarkably
588 closer to the observations and no distinct performance trends were observed for the SL
589 scheme over a diurnal cycle (Fig. 14a). This was supported by values of MAE_{sub} and
590 MAE_{day} of the same order of magnitude, as indicated in Table 4. Nonetheless, positive
591 (negative) errors were frequently observed at night (day) for the days in Table 4.
592 Westerly winds with speeds $> 5 \text{ m s}^{-1}$ were frequently observed (Fig. 13c-d), likely
593 responsible for the higher values of friction velocity and thus the higher overall skill of the
594 SL scheme for these days (Fig. 13a), as evidenced by the good agreement between the
595 observed wind speed and friction velocity for all days between 08:00-18:00 LT (Fig. 13a,
596 c).
597 As shown in Fig. 13e, the time variability of the spatial heterogeneity of the flow quantified
598 by MAD remained approximately constant over a diurnal cycle (as opposed to Fig. 11e).
599 Similarly to what we observed earlier (Fig. 11b, e), the MAD had an influence on the
600 simulation error for the days in Table 4, as evidenced by the temporal correlation between
601 the two time series in Fig. 13b, e. For these days, the magnitude of the MAD was
602 approximately the same than for days with the highest SL scheme errors indicated in Table
603 3 (Fig. 11e; Fig. 13e). Fig. 14 a-b are the analogues of Fig. 12 a-b, but corresponds to 06
604 September, which is representative of the days indicated in Table 4. The contrast between
605 Figs. 12 and 14 is remarkable. It is not clear why the MAD correlates so well with the

606 simulation error for the days when the skill of the SL scheme was the poorest (Table 3),
 607 but this correlation dropped for days where the skill of the SL scheme was the highest
 608 (Table 4), even though MAD values between -0.1 to 0.1 m s^{-1} were present in both cases.



609
 610 Figure 13: 24-hour time series of (a) Observed (dots) and simulated u_{sim}^* (solid lines) friction velocity; (b)
 611 Error; (c) Observed wind speed; (d) Wind direction (θ); and (e) Mean Absolute Deviation (MAD) of friction
 612 velocity at $z = 10$ m calculated using all towers for 08/27/16, 09/06/16, 09/17/16, and 09/19/16. The abscissa
 613 in (a)-(e) is the hour of the day in local time.

614
 615

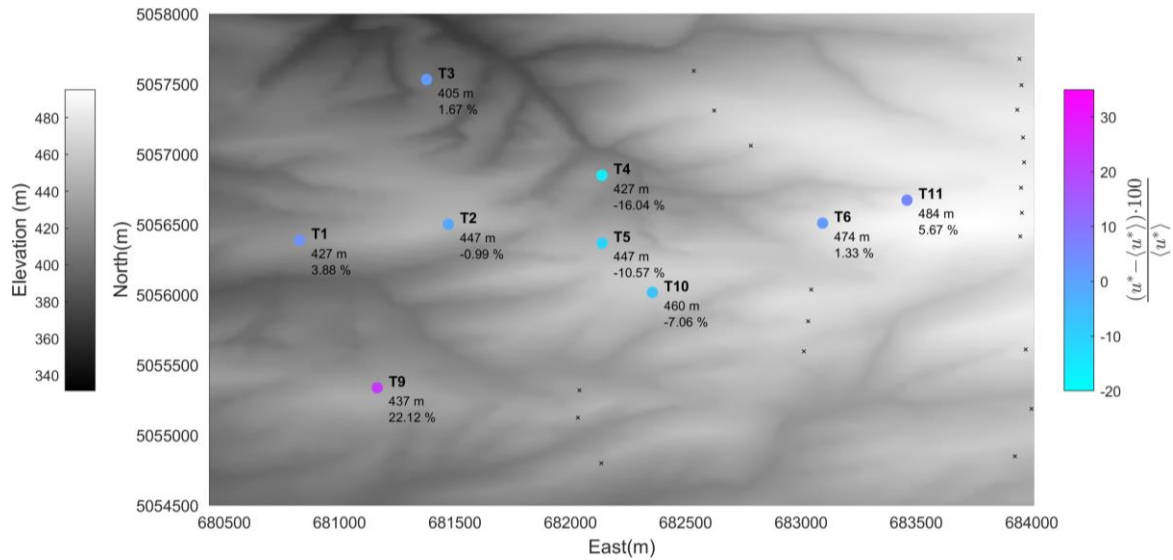


616
 617 Figure 14: 24-hour time-series for 06 September 2016. a) Error (black line with values on the left ordinate)
 618 and MAD (blue line, right ordinate); and b) Observed friction velocity at T1, T2, T6, and T11 compared with
 619 the spatially averaged observed $\langle u^* \rangle$ (blue line with markers) and simulated friction velocity u_{sim}^* (black line
 620 with markers). The abscissa in (a)-(b) is the hour of the day in local time.
 621

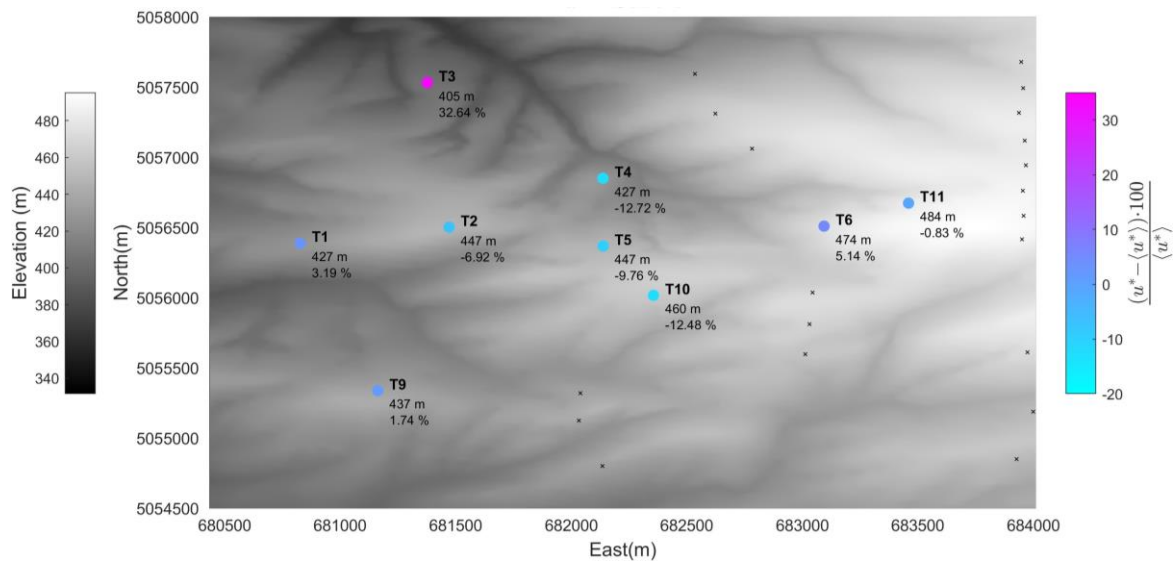
622 The percentual differences between local and spatially averaged values of u^* at $z = 10\text{m}$
 623 for unstable conditions between 12:00 – 15:00 PST for the entire observational period 27
 624 August to 26 September 2016 are shown together with the instrumented region’s elevation
 625 in Fig. 15a. Fig. 15b is analogous to Fig. 15a, but for Stable conditions between 00:00 –
 626 03:00 PST.

627 In general, spatial differences (in %) in u^* across sites were not very different between the
 628 UN and S regimes, and no clear correlations between terrain elevation and deviations
 629 between local and spatially averaged friction velocity were present, likely due to the gentle
 630 nature of the terrain (e.g., see the difference in horizontal and vertical scales in Fig. 1a),
 631 the lack of measurements in low-laying areas (except for T3), and the higher frequency of
 632 wind speeds $> 5 \text{ m s}^{-1}$ for the selected westerly winds. Nonetheless, at individual locations,
 633 deviations between u^* and $\langle u^* \rangle$ were more affected by the stability regime (UN or S), e.g.,
 634 at sites T1 and T5, these deviations remained approximately constant as the stability regime
 635 changed, whereas big differences were observed at sites T2, T6, and T11, where the
 636 proximity to local ridges could have had an influence. In addition, for the UN regime, u^*
 637 values were only $\sim 2\%$ higher than $\langle u^* \rangle$ at site T3, and $\sim 22\%$ higher at T9. Conversely,
 638 for the S regime, u^* values were $\sim 33\%$ higher than $\langle u^* \rangle$ at site T3, and $\sim 2\%$ higher than
 639 $\langle u^* \rangle$ at T9. The extent to which the terrain contributed to these alternating phenomena was
 640 beyond the scope of this work and would likely require space-resolved instrumentation
 641 (e.g., scanning lidars), or high-resolution Large Eddy Simulations (LES). For
 642 completeness, we calculated the analogous of Figs. 15a-b, but for the deviations between
 643 \overline{wT} and $\langle \overline{wT} \rangle$ (for details see Fig. A.6). For \overline{wT} , the overall heterogeneity between the UN
 644 and S regimes were similar, but the spatial variability between towers (in %) was higher
 645 and more complex than the one observed for the friction velocity.

(a) Local differences (%) between u^* and $\langle u^* \rangle$ - Unstable



(b) Local differences (%) between u^* and $\langle u^* \rangle$ - Stable



646 Figure 15: Topography of instrumented region (grayscale) and tower sites with annotated terrain elevation.
 647 The percentual differences between local and spatially averaged friction velocity at $z = 10\text{m}$ are shown for
 648 all sites. (a) Corresponds to UN periods between 12:00 – 15:00 PST for the observational period. (b) Same
 649 as before, but for Stable periods between 00:00 – 03:00 PST.

650
 651
 652
 653

654

655
 656

657 4 Discussion

658

659

▪ CFL Validity

660

661

662

663

664

665

666

667

668

669

670

671

672

673

674

For UN conditions, CFL for $\overline{w'T'}$ was satisfied about 5-10% of the time, and CFL for $\overline{u'w'}$ was satisfied ~10-20% of the time. For S conditions, CFL for $\overline{w'T'}$ was satisfied about 5-10% of the time, while CFL for $\overline{u'w'}$ was satisfied ~10% of the time. For N conditions, CFL for $\overline{w'T'}$ was satisfied (1-6%) of the time, mostly a consequence of the small number of N cases. Our results have both differences and similarities with previous studies, which are most likely due to different [largely unknown] interactions between local terrain and background flow/stability. For example, Sfyri et al. (2018) found that for unstable and stable conditions, the CFL condition is satisfied about 1% of the time for the momentum fluxes and about 50% of the time for temperature fluxes. Nadeau et al. (2013) found that in the first 6 meters above a steep slope (30-40°) in the Swiss Alps, fluxes can be more than an order of magnitude different from their ground values. Our study, however, is more detailed than the previous ones as it investigated the validity of CFL using multiple towers over a small horizontal extent (1-3 km) within a mesoscale grid cell.

673

674

▪ Fluxes Horizontal Variability

675

676

677

678

679

680

681

682

683

684

685

686

687

688

689

690

691

692

693

694

695

For convenience, a 10% threshold (Sect. 3.3) was used to identify the towers that had local fluxes ($\overline{u'w'}$, $\overline{w'T'}$) higher or lower than their spatially averaged values. For a given stability regime (UN, N or S), both ($\overline{u'w'}$) and ($\overline{w'T'}$) exhibited similar deviations with respect to their spatially averaged values, ($\langle \overline{u'w'} \rangle$) and ($\langle \overline{w'T'} \rangle$), across all tower sites. As expected, stability played a role in this variability, and the UN regime exhibited higher variability than the S regime. During N, local deviations were less than $\pm 10\%$ of the spatially averaged fluxes most of the time, but the number of N cases were infrequently reported compared to the UN and S regimes. Finally, the tower T11 exhibited unique behaviour for $\overline{u'w'}$ and $\overline{w'T'}$, where systematically higher (or lower) values were observed locally when compared to the rest of the towers, which calls for more detailed studies to investigate sub-grid variability in complex terrain when the local topographic variability is high. The average slope from the foothill to T11 in the windward face was much higher (~15%) compared to all other towers (~8%), and the configuration at T11 may have a propensity for flow separation, likely due to differences in surface roughness and the presence of upstream terrain heterogeneities where flow could pool during low wind and stable conditions. According to Walmsley & Taylor (1996), linear theories for complex terrain flows perform better for low slopes ($\leq 17^\circ$), implying flow separation and non-linear effects become important for large slopes.

693

694

695

696 ▪ Atmospheric Surface layer (ASL) Parameterizations

697 The influence of surface heterogeneity on flow and turbulence is a topic of continuing
698 interest (Stoll et al. 2020). Because of high flow variability, stability dependence of
699 meteorology and logistical constraints, complex-terrain field campaigns have not provided
700 a clear delineation of heterogeneity effects on ASL (Maronga and Raasch 2013). Only a
701 few field experiments have recorded the characteristics of flow at high horizontal
702 resolutions in complex terrain (Eder et al. 2015; Fernando et al. 2015, 2019), and our
703 present knowledge is largely derived from very high horizontal resolution Large-Eddy-
704 Simulations (LES) that has become the tool of choice for ASL studies (Chow et al. 2019;
705 Stoll et al. 2020). Our observations showed that the highest flow heterogeneity (lowest
706 parameterization scheme performance) occurs during VU conditions. Rai et al. (2017) used
707 LES to study the convective boundary layer and found that horizontal gradients play a key
708 role in the total TKE budgets in complex terrain. LES of Maronga and Raasch (2013) found
709 that surface heterogeneities may lead to ‘roll-like’ secondary circulations when wind
710 speeds are in the range 3-6 m s⁻¹, which look like ‘updrafts’ and ‘downdrafts’ across a
711 horizontal plane; this was used to explain the heterogeneous distribution of sensible heat
712 flux. In our study, such features were not recorded even though the instrumentation was
713 capable of doing so. We found that (i) flow heterogeneity may explain errors in a widely
714 used mesoscale model parameterization scheme, and (ii) under certain meteorological
715 conditions (westerly winds >5 m s⁻¹), flow heterogeneity (a time-dependent parameter) in
716 the complex terrain considered may become comparable to that of flat terrain. Thus, the
717 skill of parameterization schemes in mesoscale models can be quite effective in both cases.
718 Our findings call for further detailed field campaigns to study sub-grid variability, perhaps
719 in conjunction with high-resolution LES simulations to identify physical mechanisms
720 underlying flow heterogeneity, which will help improve surface layer parameterization
721 schemes under different background flow conditions.
722

723 **5 Summary and Conclusions**

724
725 In this article, we investigated the spatial variability of SL parameters including the
726 stability parameter (z/L^*) and the turbulent heat and momentum fluxes (\overline{wT} and \overline{uw} ,
727 respectively) over horizontal scales that are not properly resolved (subgrid) by NWP
728 models and for an area of heterogeneous terrain located in the vicinity of the Columbia
729 River in the U.S. Pacific Northwest. In addition, we explored the validity of the Constant-
730 Flux Layer (CFL) and the skill of a SL parameterization based on Monin-Obukhov (MO)
731 theory. The data used in this study was representative of the late summer/early fall
732 meteorology in the region. The measurements were quality controlled for outliers, and to
733 minimize disturbances from tower’s booms and wake effects from wind turbines located

734 in the eastern part of the domain, only winds in the sector $240^\circ - 290^\circ$ were considered in
735 the results of Sects. 3.2- 3.4.

736 Our analysis showed that the validity of the CFL concept was dependent on: (i) the
737 turbulent parameter being analysed, (ii) the measurement's location (along the east-west
738 transect), (iii) the atmospheric stability regime, and (iv) the magnitude of the flux. To
739 evaluate the validity of the CFL for the momentum and temperature fluxes, we adopted a
740 10% threshold based on the study of Sfyri et al. (2018). Monin Obukhov (MO) equations
741 used in WRF SL option 2 (Jiménez et al. 2012a,b) were used to simulate time series of
742 friction velocity for 27 August to 26 September 2016. MO theory assumes the existence of
743 a CFL and horizontally homogeneity of flow. Naturally, the expectation was that MO
744 would fail in view of terrain heterogeneity. Higher errors in the SL scheme were associated
745 with high flow heterogeneity, as quantified by the Mean Absolute Deviation (MAD)
746 between the simulated and observed friction velocity. Notwithstanding, on the days with
747 transitional westerly winds ($>5 \text{ m s}^{-1}$), the parameterization scheme predicted the observed
748 friction velocity remarkably well ($< 20\%$ errors).

749 This paper is dedicated to the memory of a prominent meteorologist and an excellent
750 mentor Professor Sergej S. Zilitinkevich, and it is written for this Special Issue in his
751 honour. For over 50 years, Prof. Sergej Zilitinkevich carried out pioneering research on
752 atmospheric turbulence and planetary boundary layer (PBL). Among his numerous
753 outstanding achievements in atmospheric boundary layer theory, a few results should be
754 highlighted in relation to this study. At the end of the 1960s, Zilitinkevich and Chalikov
755 (1968) proposed a simple linear interpolation (log-linear law) for the non-dimensional
756 vertical gradient of mean wind speed (\bar{u}) that provides blending between neutral and very
757 stable ('z-less') cases. The WRF modelers undoubtedly appreciate Sergej's works through
758 the " C_{zil} coefficient", which represents the coupling between the aerodynamic z_0 (see Eq.
759 4) and scalar z_{0t} (e.g., temperature and water vapour) roughness lengths (Zilitinkevich
760 1970; Zilitinkevich et al. 1992, 2001 and references therein). Here it is impossible not to
761 mention some of his other achievements and contributions to the field: the depth of the
762 stably stratified PBL, the resistance and heat and mass transfer laws for geophysical
763 turbulent flows (Zilitinkevich 1970), non-local theory of the atmospheric PBL (e.g.,
764 Zilitinkevich et al. 2006), and higher-order turbulence parameterization schemes
765 (Zilitinkevich et al. 2013), to name a few.

Acknowledgments: University of Notre Dame contribution to WFIP2 project was funded by the grant DOE-WFIP2-SUB-001. The work appearing in this paper was supported by the US National Science Foundation Award AGS-1921554.

Data Statement: The datasets analysed during the current study are available in the WFP2 repository of the Atmosphere to Electrons Data archive of the U.S. Department of Energy and is publicly available to download at <https://a2e.energy.gov/projects/wfip2>

766 6 References

767

- 768 Bodini, N., Lundquist, J. K., Krishnamurthy, R., Pekour, M., Berg, L. K., & Choukulkar,
769 A. (2019). Spatial and temporal variability of turbulence dissipation rate in complex
770 terrain. *Atmospheric Chemistry and Physics*, 19(7), 4367-4382.
- 771 Carvalho L, Duine GJ, Jones C, et al (2020) The Sundowner Winds Experiment (SWEX)
772 pilot study: Understanding downslope windstorms in the Santa Ynez Mountains,
773 Santa Barbara, California. *Mon Weather Rev* 148:1519–1539.
774 <https://doi.org/10.1175/MWR-D-19-0207.1>
- 775 Chung U, Seo HH, Hwang KH, et al (2006) Minimum temperature mapping over
776 complex terrain by estimating cold air accumulation potential. *Agric For Meteorol*
777 137:15–24. <https://doi.org/10.1016/j.agrformet.2005.12.011>
- 778 Li, D., Katul, G. G., & Liu, H. (2018). Intrinsic constraints on asymmetric turbulent
779 transport of scalars within the constant flux layer of the lower
780 atmosphere. *Geophysical Research Letters*, 45(4), 2022-2030.
- 781 Eder F, Schmidt M, Damian T, et al (2015) Mesoscale eddies affect near-surface
782 turbulent exchange: Evidence from lidar and tower measurements. *J Appl Meteorol*
783 *Climatol* 54:189–206. <https://doi.org/10.1175/JAMC-D-14-0140.1>
- 784 Fernando HJS (2010) Fluid Dynamics of Urban Atmospheres in Complex Terrain. *Annu*
785 *Rev Fluid Mech* 42:365–389. <https://doi.org/10.1146/annurev-fluid-121108-145459>
- 786 Fernando HJS, Mann J, Palma JMLM, et al (2019) The Perdigao Peering into Microscale
787 Details of Mountain Winds. *Bull Am Meteorol Soc* 799–820.
788 <https://doi.org/10.1175/BAMS-D-17-0227.1>
- 789 Fernando HJS, Pardyjak ER, Di Sabatino S, et al (2015) Unraveling the Intricacies of
790 Mountain Weather. *Bull Am Meteorol Soc* 1945–1968.
791 <https://doi.org/10.1175/BAMS-D-13-00131.1>
- 792 Garratt, J., 1994. The atmospheric boundary layer. *Earth Sci. Rev.* 37 (1–2), 89–134.
793 https://doi.org/10.1007/3-211-38078-7_4.
- 794 Giovannini L, Ferrero E, Karl T, et al (2020) Atmospheric pollutant dispersion over
795 complex terrain: Challenges and needs for improving air quality measurements and
796 modeling. *Atmosphere (Basel)* 11:1–32. <https://doi.org/10.3390/atmos11060646>
- 797 Grachev, A.A., Fairall, C.W., Persson, P.O.G., Andreas, E.L, Guest, P.S. (2005) Stable
798 boundary-layer scaling regimes: The SHEBA data. *Boundary-Layer Meteorol.*
799 116(2), 201–235. <https://doi.org/10.1007/s10546-004-2729-0>
- 800 Grachev A.A., Fairall C.W., Blomquist B.W., Fernando H.J.S., Leo L.S., Otárola-Bustos
801 S.F., Wilczak J.M., McCaffrey K.L. (2020) On the surface energy balance closure at
802 different temporal scales. *Agric. Forest Meteorol.* 281:
803 <https://doi.org/10.1016/j.agrformet.2019.107823>
- 804 Grachev, A. A., Fairall, C. W., Blomquist, B. W., Fernando, H. J., Leo, L. S., Otárola-
805 Bustos, S. F., ... & McCaffrey, K. L. (2022). A Hybrid Bulk Algorithm to Predict

806 Turbulent Fluxes over Dry and Wet Bare Soils. *Journal of Applied Meteorology and*
807 *Climatology*, 61(4), 393-414.

808 Grell, G. A. , Dudhia, J., and Stauffer, D. R., 1995, A Description of the Fifth-
809 Generation Penn State/NCAR Mesoscale Model (MM5) NCAR Technical Note,
810 NCAR/TN-398+STR, Boulder, CO., 138 pp.

811 Gultepe I, Sharman R, Williams PD, et al (2019) A Review of High Impact Weather for
812 Aviation Meteorology. *Pure Appl Geophys* 176:1869–1921.
813 <https://doi.org/10.1007/s00024-019-02168-6>

814 Haupt SE, Kosovic B, Shaw W, et al (2019) On bridging a modeling scale gap:
815 Mesoscale to microscale coupling for wind energy. *Bull Am Meteorol Soc*
816 100:2533–2549. <https://doi.org/10.1175/BAMS-D-18-0033.1>

817 Hong S-Y, Dudhia J (2012) Next-Generation Numerical Weather Prediction: Bridging
818 Parameterization, Explicit Clouds, and Large Eddies. *Bull Am Meteorol Soc*
819 93:ES6–ES9. <https://doi.org/10.1175/2011bams3224.1>

820 Jiménez PA, Dudhia J, González-Rouco JF, et al (2012a) A revised scheme for the WRF
821 surface layer formulation. *Mon Weather Rev* 140:898–918.
822 <https://doi.org/10.1175/MWR-D-11-00056.1>

823 Jiménez PA, Dudhia J, González-Rouco JF, et al (2012b) A Revised Scheme for the
824 WRF Surface Layer Formulation. *Mon Weather Rev* 140:898–918.
825 <https://doi.org/10.1175/MWR-D-11-00056.1>

826 Kadivar, M., Tormey, D., & McGranaghan, G. (2021). A review on turbulent flow over
827 rough surfaces: Fundamentals and theories. *International Journal of*
828 *Thermofluids*, 10, 100077.

829 Kaimal, J. C., & Businger, J. A. (1970) Case studies of a convective plume and a dust
830 devil. *Journal of Applied Meteorology and Climatology*, 9(4), 612-620.

831 Klipp, C. L., & Mahrt, L. (2004). Flux–gradient relationship, self-correlation and
832 intermittency in the stable boundary layer. *Quarterly Journal of the Royal*
833 *Meteorological Society: A journal of the atmospheric sciences, applied meteorology*
834 *and physical oceanography*, 130(601), 2087-2103.

835 Liang J, Guo Q, Zhang Z, et al (2020) Influence of complex terrain on near-surface
836 turbulence structures over loess plateau. *Atmosphere (Basel)* 11:.
837 <https://doi.org/10.3390/atmos11090930>

838 Luchetti NT, Friedrich K, Rodell CE, Lundquist JK (2020) Characterizing thunderstorm
839 gust fronts near complex terrain. *Mon Weather Rev* 148:3267–3286.
840 <https://doi.org/10.1175/MWR-D-19-0316.1>

841 Mahrt L., Thomas C.K., Grachev A., Persson P.O.G. (2018) Near-surface vertical flux
842 divergence in the stable boundary layer. *Boundary-Layer Meteorol.* 169 (3): 373–
843 393. <https://doi.org/10.1007/s10546-018-0379-x>

844 Maronga B, Knigge C, Raasch S (2020) An Improved Surface Boundary Condition for
845 Large-Eddy Simulations Based on Monin–Obukhov Similarity Theory: Evaluation

846 and Consequences for Grid Convergence in Neutral and Stable Conditions.
847 Boundary-Layer Meteorol 174:297–325. <https://doi.org/10.1007/s10546-019-00485>
848 w

849 Maronga B, Raasch S (2013) Large-Eddy Simulations of Surface Heterogeneity Effects
850 on the Convective Boundary Layer During the LITFASS-2003 Experiment.
851 Boundary-Layer Meteorol 146:17–44. <https://doi.org/10.1007/s10546-012-9748-z>
852 Martins CA, Moraes OLL, Acevedo OC, Degrazia GA (2009) Turbulence intensity
853 parameters over a very complex terrain. Boundary-Layer Meteorol 133:35–45.
854 <https://doi.org/10.1007/s10546-009-9413-3>

855 Monin, A. S., & Obukhov, A. M. (1954). Basic laws of turbulent mixing in the surface
856 layer of the atmosphere. Contrib. Geophys. Inst. Acad. Sci. USSR, 151(163), e187.

857 Moraes, O. L., Acevedo, O. C., Degrazia, G. A., Anfossi, D., da Silva, R., & Anabor, V.
858 (2005). Surface layer turbulence parameters over a complex terrain. Atmospheric
859 Environment, 39(17), 3103-3112.

860 Muñoz-Esparza D, Cañadillas B, Neumann T, Van Beeck J (2012) Turbulent fluxes,
861 stability and shear in the offshore environment: Mesoscale modelling and field
862 observations at FINO1. J Renew Sustain Energy 4:.
863 <https://doi.org/10.1063/1.4769201>

864 Nadeau DF, Pardyjak ER, Higgins CW, Parlange MB (2013) Similarity Scaling Over a
865 Steep Alpine Slope. Boundary-Layer Meteorol 147:401–419.
866 <https://doi.org/10.1007/s10546-012-9787-5>

867 Nakanishi M, Niino H (2009) Development of an Improved Turbulence Closure Model
868 for the Atmospheric Boundary Layer. J Meteorol Soc Japan 87:895–912.
869 <https://doi.org/10.2151/jmsj.87.895>

870 Obukhov, A. (1946) Turbulence in thermally inhomogeneous atmosphere. Trudy Inst.
871 Teor. Geofiz. Akad. Nauk SSSR, 1, 95-115.

872 Panofsky a. (1962) Determination of stress from wind. Q J R Meteorol Soc

873 Panofsky HA and Dutton JA (1984) Atmospheric Turbulence - Models and Methods for
874 Engineering Applications. John Wiley and Sons, New York, 397 pp.
875

876 Rai RK, Berg LK, Pekour M, et al (2017) Spatiotemporal variability of turbulence kinetic
877 energy budgets in the convective boundary layer over both simple and complex terrain. J
878 Appl Meteorol Climatol 56:3285–3302. <https://doi.org/10.1175/JAMC-D-17-0124.1>

879 Sati AP, Mohan M (2021) Impact of urban sprawls on thunderstorm episodes:
880 Assessment using WRF model over central-national capital region of India. Urban
881 Clim 37:100869. <https://doi.org/10.1016/j.uclim.2021.100869>

882 Sfyri E, Rotach MW, Stiperski I, et al (2018) Scalar-Flux Similarity in the Layer Near the
883 Surface Over Mountainous Terrain. Boundary-Layer Meteorol 169:11–46.
884 <https://doi.org/10.1007/s10546-018-0365-3>

885 Skamarock WC, Klemp J.B, Dudhia J., Gill D.O, Barker D.M, Duda M.G, Huang X.-

886 Y., Wang W., Powers J.G. A Description of the Advanced Research WRF Version
887 3, National Center for Atmospheric Research Technical Note
888 NCAR, Boulder (2008) http://www.mmm.ucar.edu/wrf/users/docs/arw_v3.pdf
889 Stoll R, Gibbs JA, Salesky ST, et al (2020) Large-Eddy Simulation of the Atmospheric
890 Boundary Layer. *Boundary-Layer Meteorol* 177:541–581.
891 <https://doi.org/10.1007/s10546-020-00556-3>
892 Stull, R. B. (1988). An introduction to boundary layer meteorology (Vol. 13). Springer
893 Science & Business Media.
894 Tampieri, F., Maurizi, A., & Viola, A. (2009). An investigation on temperature variance
895 scaling in the atmospheric surface layer. *Boundary-layer meteorology*, 132(1), 31-
896 42.
897 Walmsley, J. L., and Taylor, P. A., 1996: Boundary-layer flow over topography: impacts
898 of the Askervein study, *Boundary-Layer Meteor.*, 78(3-4), 291-320;
899 DOI:10.1007/BF00120939.
900 Wilczak, J. M., et al., 2019: The Second Wind Forecast Improvement Project (WFIP2):
901 Observational Field Campaign. *Bull. Amer. Meteor. Soc.*,
902 <https://doi.org/10.1175/BAMS-D-18-0035.1>.
903 Wilczak, J. M., Oncley, S. P., & Stage, S. A. (2001). Sonic anemometer tilt correction
904 algorithms. *Boundary-layer meteorology*, 99(1), 127-150.
905 Wouters H, de Ridder K, van Lipzig NPM (2012) Comprehensive Parametrization of
906 Surface-Layer Transfer Coefficients for Use in Atmospheric Numerical Models.
907 *Boundary-Layer Meteorol* 145:539–550. <https://doi.org/10.1007/s10546-012-9744-3>
908 Wyngaard JC (2011) The atmospheric surface layer. *Turbul Atmos* 215–240.
909 <https://doi.org/10.1017/cbo9780511840524.011>
910 Zilitinkevich, S. S., & Chalikov, D. V. (1968). The laws of resistance and of heat and
911 moisture exchange in the interaction between the atmosphere and an underlying
912 surface. *Izv. Acad. Sci., USSR., Atmospheric and Oceanic Phys*, 4, 765-772.
913 Zilitinkevich SS (1970) Dynamics of the atmospheric boundary layer. *Gidrometeoizdat*.
914 Leningrad, 290 pp
915 Zilitinkevich S.S., Fedorovich E.E., Shabalova M.V. (1992) Numerical model of a non-
916 steady atmospheric planetary boundary layer, based on similarity theory. *Boundary-
917 Layer Meteorol.* 59(4): 387–411. <https://doi.org/10.1007/BF02215460>
918 Zilitinkevich S.S., Grachev A.A., Fairall C.W. (2001) Scaling reasoning and field data on
919 the sea-surface roughness lengths for scalars. *J. Atmos. Sci.* 58(3), 320–325.
920 Zilitinkevich S.S., Hunt J.C.R., Esau I.N., Grachev A.A., Lalas D.P., Akylas E., Tombrou
921 M., Fairall C.W., Fernando H.J.S., Baklanov A.A., Joffre S.M. (2006) The influence
922 of large convective eddies on the surface layer turbulence. *Quart. J. Roy. Met. Soc.*,
923 132(618A), 1423–1456. <https://doi.org/10.1256/qj.05.79>
924 Zilitinkevich S.S., Elperin T., Kleerorin N., Rogachevskii I., Esau I. (2013) A hierarchy of
925 energy - and flux-budget (FEB) turbulence closure models for stably-stratified

926 geophysical flows, *Boundary-Layer Meteorol.* 146(3): 341–373.
927 <https://doi.org/10.1007/s10546-012-9768-8>

928

929

930

931

932

933

934

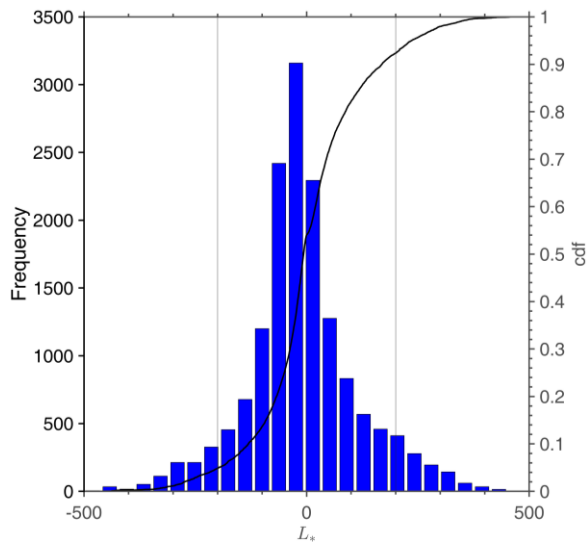
935

936

937

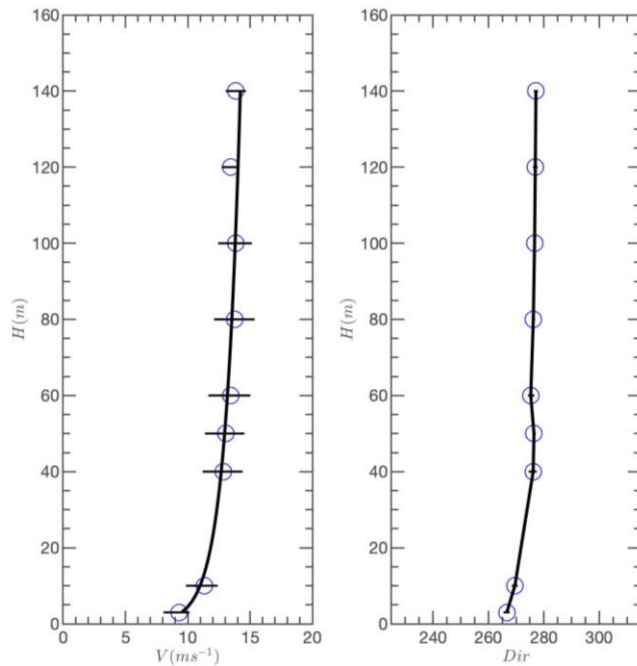
938 **Appendix:**

939

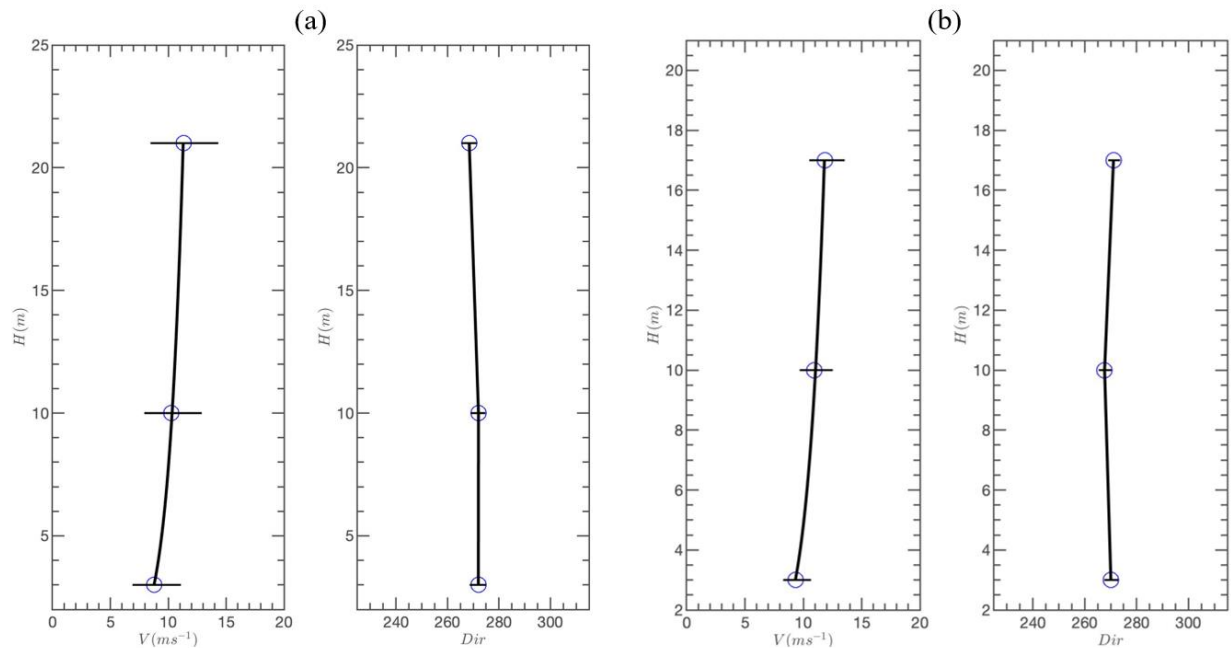


940

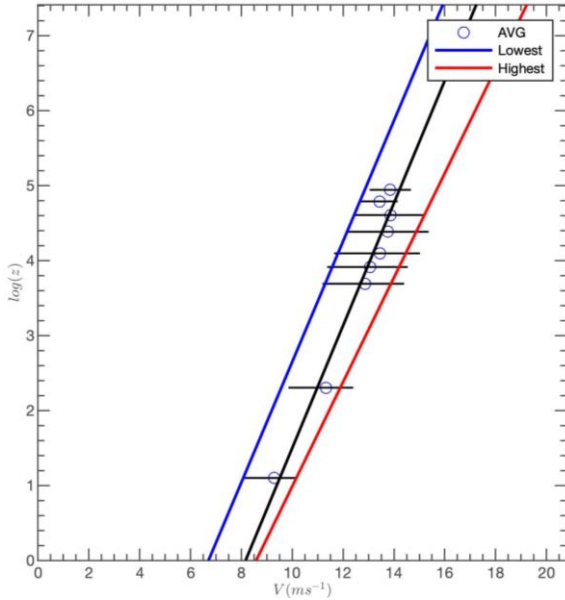
941 Figure A.1: Histogram of the Obukhov length scale using the combined measurements from all tower sites
942 at $z=10\text{m}$ agl. The two vertical lines show the lower and upper thresholds used to identify Near-Neutral (NN)
943 cases ($L_{TR} = 200$). This distribution corresponds to the wind sector (240, 290).
944



945
 946 Figure A.2: Wind speed and wind direction profiles from the combined measurements from the tower and
 947 the Sodar at site T1 that were used to estimate the roughness length value. This profile was aggregated for
 948 multiple periods with Near-Neutral (NN) conditions and the measured standard deviation is indicated by the
 949 black horizontal lines.
 950
 951

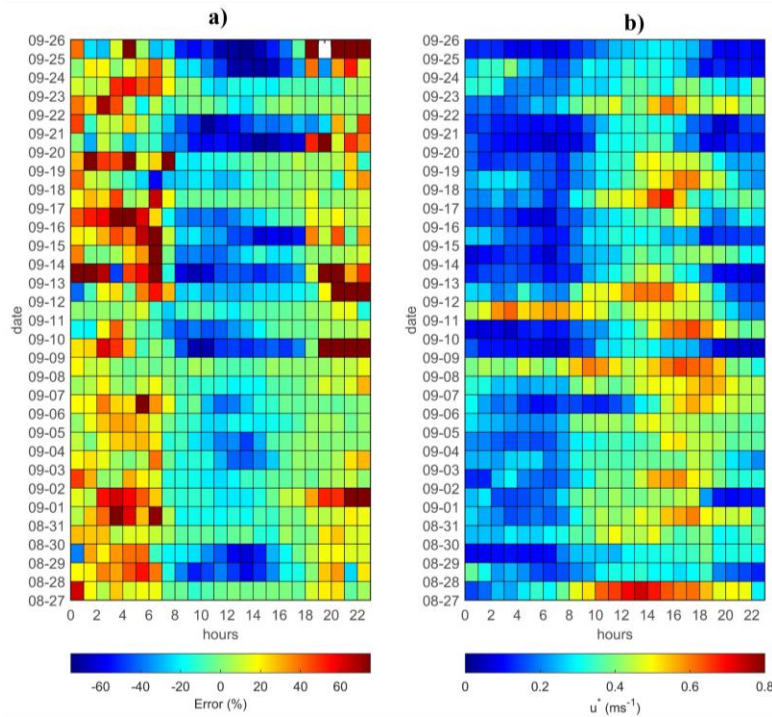


952
 953 Figure A.3: Aggregated a) wind speed and wind direction profiles measured at site T2 for NN conditions and
 954 used to calculate the roughness length at site T2, and b) Same as in (a) but for site T6. The standard deviation
 955 is indicated by the black horizontal line.
 956



957
958
959
960

Figure A.4: An example of the methodology proposed by Panofsky (1962) to determine roughness length. The methodology was applied to the velocity profiles measured at site T1 (as shown in Fig. A. 2).

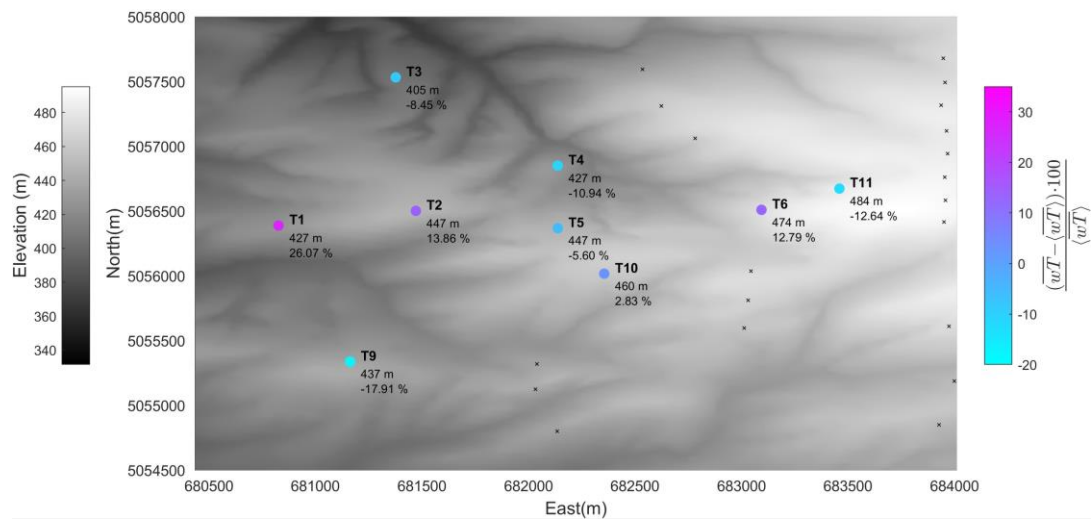


961
962
963
964
965
966
967
968

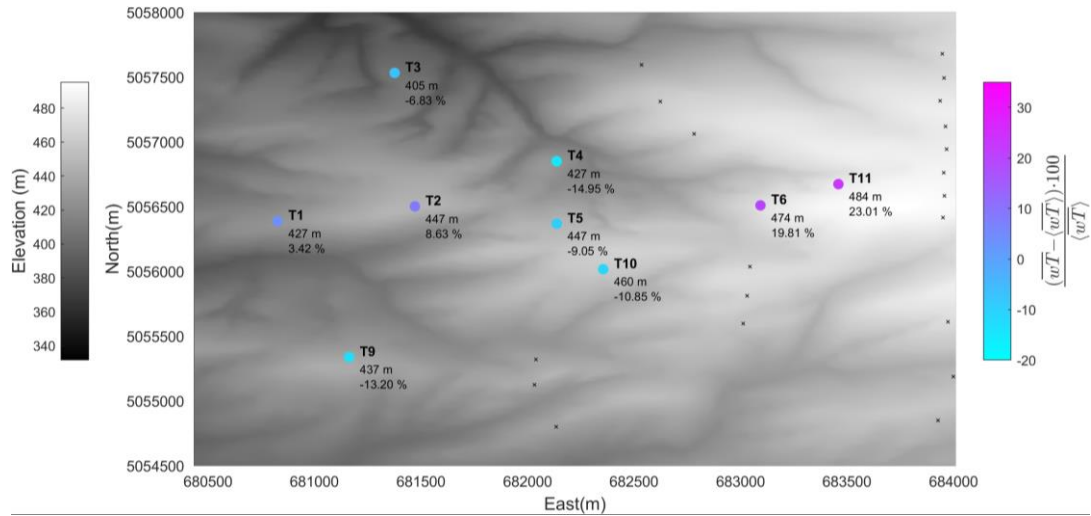
Figure A.5: Color maps of (a) 1h Error (%) between observed and simulated friction velocities; and (b) 1h observed friction velocity for the period 27 August 2016 to 26 September 2016. The abscissa indicates the local time whereas the ordinate is the date.

969
970
971
972
973
974
975
976
977
978
979
980

(a) Local differences between \overline{wT} and $\langle \overline{wT} \rangle$ - Unstable



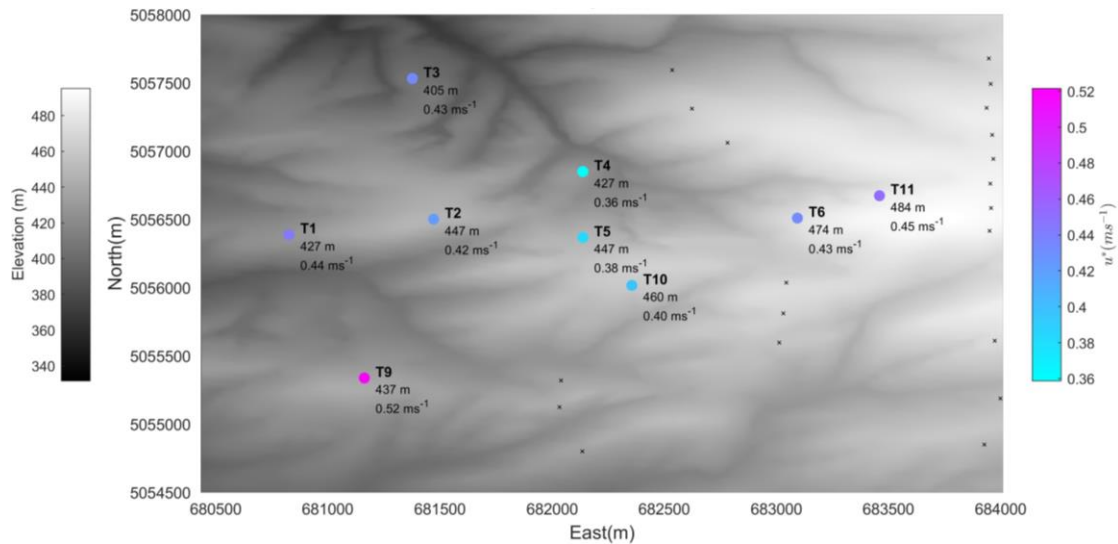
(b) Local differences between \overline{wT} and $\langle \overline{wT} \rangle$ - Stable



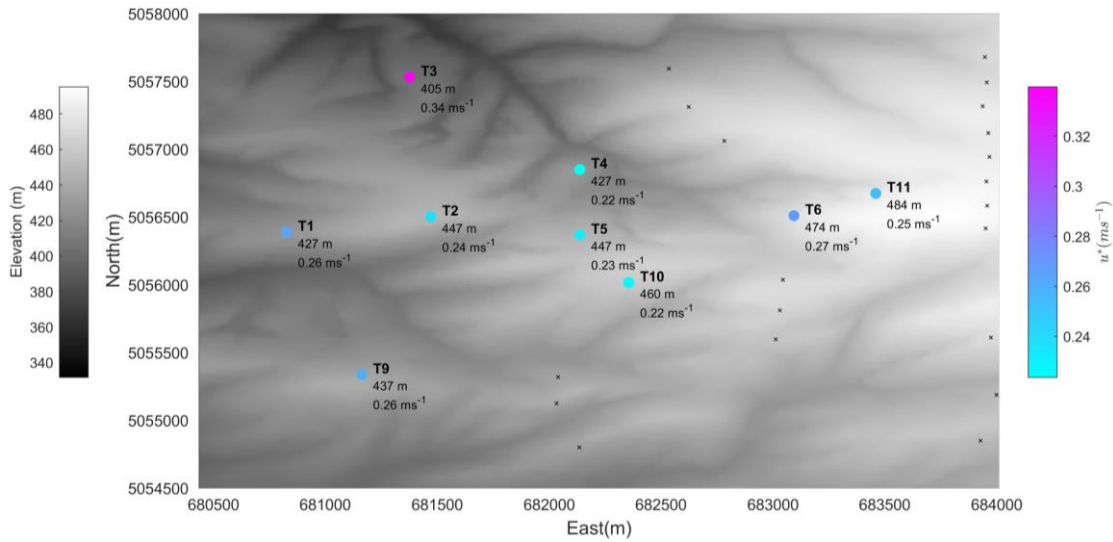
981 Figure A.6: Topography of instrumented region (grayscale) and tower sites with annotated terrain elevation.
 982 The percentual differences between local and spatially averaged temperature fluxes at $z = 10\text{m}$ are shown for
 983 all sites. (a) Corresponds to UN periods between 12:00 – 15:00 PST for the observational period. (b) Same
 984 as before, but for Stable periods between 00:00 – 03:00 PST.

985
 986
 987
 988
 989
 990
 991
 992
 993
 994

(a) Local values of u^* - Unstable

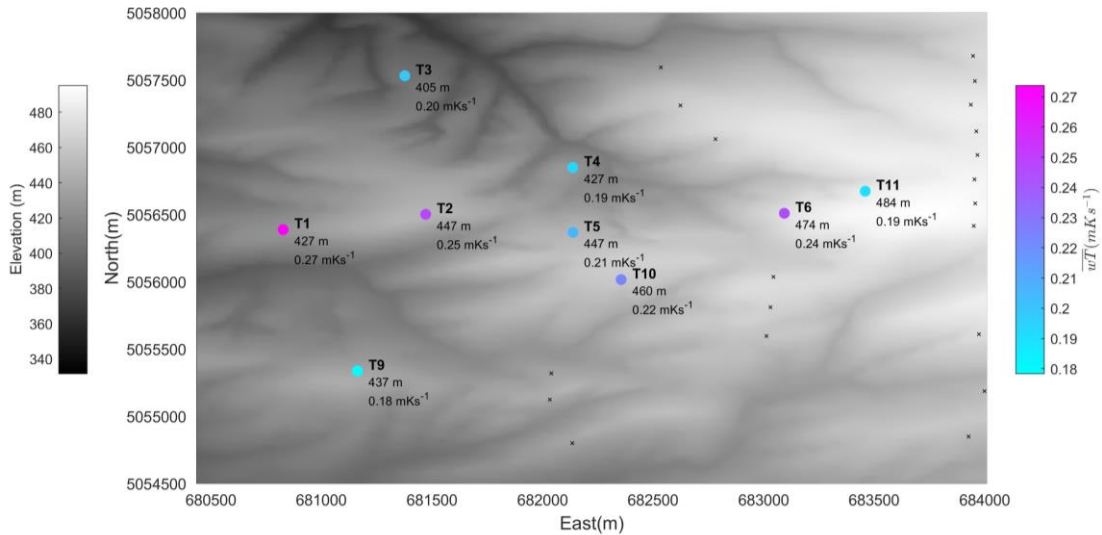


(b) Local values of u^* - Stable

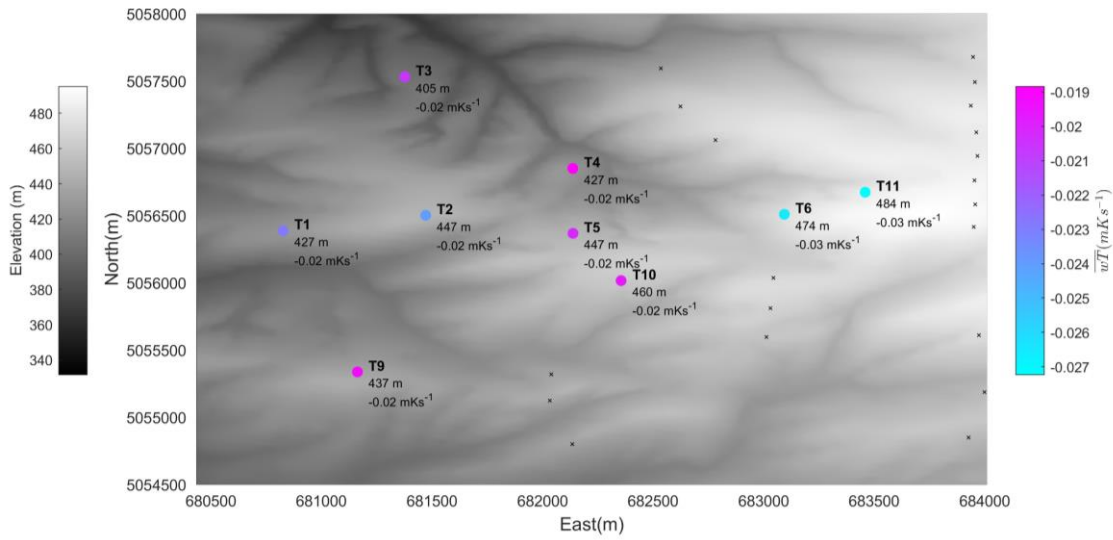


995
 996
 997
 998
 999
 1000
 1001
 1002
 1003
 1004
 1005
 1006
 1007

(a) Local values of \overline{wT} - Unstable



(b) Local values of \overline{wT} - Stable



1008 Figure A.8: Topography of instrumented region (grayscale) and tower sites with annotated terrain elevation.
 1009 Local values of temperature fluxes (\overline{wT}) at $z = 10$ m are shown for all sites. (a) Corresponds to UN periods
 1010 between 12:00 – 15:00 PST for the observational period. (b) Same as before, but for Stable periods between
 1011 00:00 – 03:00 PST
 1012
 1013

References

- Bodini, N., Lundquist, J. K., Krishnamurthy, R., Pekour, M., Berg, L. K., & Choukulkar, A. (2019). Spatial and temporal variability of turbulence dissipation rate in complex terrain. *Atmospheric Chemistry and Physics*, 19(7), 4367-4382.
- Klipp, C. L., & Mahrt, L. (2004). Flux–gradient relationship, self-correlation and intermittency in the stable boundary layer. *Quarterly Journal of the Royal Meteorological Society: A journal of the atmospheric sciences, applied meteorology and physical oceanography*, 130(601), 2087-2103.
- Li, D., Katul, G. G., & Liu, H. (2018). Intrinsic constraints on asymmetric turbulent transport of scalars within the constant flux layer of the lower atmosphere. *Geophysical Research Letters*, 45(4), 2022-2030.
- Muñoz-Esparza D, Cañadillas B, Neumann T, Van Beeck J (2012) Turbulent fluxes, stability and shear in the offshore environment: Mesoscale modelling and field observations at FINO1. *J Renew Sustain Energy* 4:. <https://doi.org/10.1063/1.4769201>
- Sfyri E, Rotach MW, Stiperski I, et al (2018) Scalar-Flux Similarity in the Layer Near the Surface Over Mountainous Terrain. *Boundary-Layer Meteorol* 169:11–46. <https://doi.org/10.1007/s10546-018-0365-3>
- Tampieri, F., Maurizi, A., & Viola, A. (2009). An investigation on temperature variance scaling in the atmospheric surface layer. *Boundary-layer meteorology*, 132(1), 31-42.